A ciliopathy complex builds distal appendages to initiate ciliogenesis

Dhivya Kumar[1], Addison Rains[2], Vicente Herranz-Pérez[3,4] , Quanlong Lu[11], Xiaoyu Shi[5,6], Danielle L. Swaney[8,9,10], Erica Stevenson[8,9,10], Nevan J. Krogan[8,9,10] , Bo Huang[5,7], Christopher Westlake[11], Jose Manuel Garcia-Verdugo[3], Bradley Yoder[2] and Jeremy F. Reiter[1,7]

[1]Department of Biochemistry and Biophysics, Cardiovascular Research Institute, University of California, San Francisco, San Francisco, CA, USA

[2]Department of Cell, Developmental, and Integrative Biology, University of Alabama, Birmingham

[3]Laboratory of Comparative Neurobiology, Cavanilles Institute of Biodiversity and Evolutionary Biology, University of Valencia, CIBERNED, 46980 Valencia, Spain

[4]Predepartamental Unit of Medicine, Faculty of Health Sciences, Universitat Jaume I, 12071 Castelló de la Plana, Spain

[5]Department of Pharmaceutical Chemistry, University of California, San Francisco, San Francisco, CA 94143 USA

[6]Department of Developmental and Cell Biology, University of California Irvine, Irvine, CA 92697 USA

[7]Chan Zuckerberg Biohub, San Francisco, CA 94158, USA

[8]Department of Cellular and Molecular Pharmacology, University of California, San Francisco, San Francisco, CA 94158, USA

[9]California Institute for Quantitative Biosciences, QBI, University of California, San Francisco, San Francisco, CA 94158, USA

[10]J. David Gladstone Institutes, San Francisco, CA 94158, USA

[11]Center for Cancer Research, NCI Frederick, Laboratory of Cellular and Developmental Signaling, Frederick, MD 21702, USA.

*Correspondence: Jeremy.Reiter@ucsf.edu

Running Title: The distal centriole supports ciliogenesis

ABSTRACT

Cells inherit two centrioles, the older of which is uniquely capable of generating a cilium. We identified that three evolutionarily conserved proteins that underlie human ciliopathies, CEP90, MNR and OFD1, form a complex. This complex localized to both distal centrioles and centriolar satellites, proteinaceous granules surrounding centrioles. Cells and mice lacking CEP90 or MNR did not generate cilia, failed to assemble distal appendages, and did not transduce Hedgehog signals. Disrupting the satellite pools did not affect distal appendage assembly, indicating that it is the centriolar populations of MNR and CEP90 that are critical for ciliogenesis. CEP90 recruited the most proximal known distal appendage component, CEP83, to root distal appendages formation, an early step in ciliogenesis. In addition to distal appendage formation, MNR, but not CEP90, restricted centriolar length by recruiting OFD1. We conclude that a complex of disease-associated proteins, MNR, OFD1 and CEP90, acts at the distal centriole to support ciliogenesis by restraining centriole length and assembling distal appendages.

KEYWORDS: mother centriole, distal appendages, expansion microscopy, centriole length, centriolar satellites

INTRODUCTION

Centrioles are ancient, microtubule-based structures with two main functions: first, they are core components of the centrosome, the primary microtubule organizing center, and, second, they are the foundations for cilia, cellular antennae specialized for signaling. While the main barrel of each centriole is comprised of nine radially arranged microtubule triplets, many proteins apart from tubulin comprise the centrioles (Winey and O'Toole, 2014; Keller et al., 2005, 2009; Jakobsen et al., 2011; Andersen et al., 2003). To date, the parts list of centrioles is incomplete.

Centriole structure can vary between species, but within a particular cell type, centriole length is nearly uniform, as are centriolar number and timing of assembly (Goehring and Hyman, 2012; Kong et al., 2020). Coordination with the cell cycle entrains this uniformity: centrioles duplicate during interphase and, at mitosis, each daughter cell inherits an older, mother centriole and a younger, daughter centriole (Nigg and Holland, 2018; Breslow and Holland, 2019).

The differences in centriolar age dictates different structures and functions. Only the mother centriole can assemble a cilium, and only it possesses subdistal and distal appendages. Through the distal appendages, the mother centriole attaches to pre-ciliary vesicles, an early step in ciliogenesis (Tanos et al., 2013; Sillibourne et al., 2013; Schmidt et al., 2012b). In contrast, sub-distal appendages are dispensable for ciliogenesis (Tanos et al., 2013; Mazo et al., 2016; Chong et al., 2020). Although components of appendages have been identified (Bowler et al., 2019; Yang et al., 2018; Chong et al., 2020), how they are assembled remains enigmatic.

Related to their roles in fundamental cellular processes such as cell division and intercellular communication, centriole dysfunction causes diverse human developmental disorders including ciliopathies and microcephaly (Nigg and Holland, 2018; Reiter and Leroux, 2017). For example, mutations in *CEP90* (*Centrosomal protein of 90 kDa*, also known as *PIBF1*), *MNR* (*MOONRAKER*, also known as *KIAA0753* or *OFIP*) or *OFD1* cause Joubert syndrome (JBTS), a ciliopathy characterized by brainstem and cerebellar malformations (Wheway et al., 2015; Shen et al., 2020; Hebbar et al., 2018; Stephen et al., 2017; Hammarsjö et al., 2017; Coene et al., 2009). Similarly, in many cancers, the number or structure of centrioles is dysregulated (Gönczy, 2015; Marteil et al., 2018).

CEP90 has been identified as a component of centriolar satellites, protein assemblies that orbit the centrosome (Kim et al., 2012; Kodani et al., 2015). Knockdown of *CEP90* alters the localization of centriolar satellites, which has been proposed to compromise ciliogenesis (Kim and Rhee, 2011; Kim et al., 2012).

We have used a combination of label retention expansion microscopy and structured illumination microscopy (LR-ExSIM) (Shi et al., 2019) and found that, in addition to being a

102 component of centriolar satellites, CEP90 is a component of the distal end of centrioles. Proteomic
103 analyses revealed that CEP90 is part of an evolutionarily conserved complex that includes MNR
104 and OFD1. Mouse genetic studies revealed that CEP90 and MNR are key regulators of mother
105 centriole function, essential for normal vertebrate development, Hedgehog signaling and
106 ciliogenesis. In investigating how CEP90 and MNR function in ciliogenesis, we found that both
107 are required for the assembly of distal appendages. Mutant analysis demonstrated that the
108 components of this distal centriole complex are recruited to the centriole in a hierarchical manner,
109 culminating in CEP90, which recruits the most proximal distal appendage protein, CEP83, to
110 initiate distal appendage formation. Thus, our work identifies a complex of evolutionarily ancient
111 proteins that functions at the distal mother centriole to build distal appendages, an early and
112 critical step in ciliogenesis.
113

114 **RESULTS**

115 **CEP90 localizes to centriolar satellites and a ring at the distal ends of centrioles**

116 CEP90 has previously been identified as a component of centriolar satellites (Kim and
117 Rhee, 2011). We confirmed that CEP90 localizes to centriolar satellites by immunostaining human
118 retinal pigment epithelial (RPE1) cells with antibodies to CEP90 and PCM1, a marker of centriolar
119 satellites (Fig. 1a). In addition, a centrosomal pool of CEP90 did not co-localize with PCM1 (Fig.
120 1a). To more precisely identify where centrosomal CEP90 localized, we dispersed centriolar
121 satellites with nocodazole and found that CEP90 localized with γ-tubulin at centrioles (Fig. 1b).
122 Three-dimensional structured illumination microscopy (3D-SIM) revealed that CEP90 forms rings
123 at centrioles (Fig. 1b).

124 Independent of nocodazole, we disrupted centriolar satellites in RPE1 cells by deleting
125 PCM1, a scaffold for centriolar satellites, using CRISPR/Cas9 (Supplementary Fig 1). As
126 described previously, centriolar satellites were not detected in *PCM1*$^{-/-}$ RPE1 cells (Odabasi et
127 al., 2019). Consistent with the loss of satellites, localization of CEP90 to puncta around the
128 centrosome was absent in *PCM1*$^{-/-}$ RPE1 cells (Fig. 1c). As in nocodazole-treated cells, the rings
129 of CEP90 at centrioles remained in *PCM1*$^{-/-}$ RPE1 cells (Fig. 1c), indicating that CEP90 localizes
130 to centrioles independently of PCM1 and centriolar satellites.

131 Expansion microscopy involves physically expanding samples embedded in a hydrogel
132 (Wassie et al., 2019). To precisely map the localization of CEP90 at centrioles, we combined
133 expansion microscopy together with multi-color label retention and SIM (LR-ExSIM) to minimize
134 signal loss during expansion and provide ~30 nm lateral resolution (Shi et al., 2019). The distal
135 appendage component CEP164 imaged by LR-ExSIM was comparable to data previously

136 obtained using STORM: CEP164 formed a discontinuous ring at the mother centriole (Shi et al.,
137 2019, 2017). Intriguingly, LR-ExSIM resolved that the ring of CEP90 is comprised of discrete
138 puncta with a mode of nine and separated by a mean angle of ~ 36 nm (Fig. 1d-g). In agreement
139 with 3D-SIM microscopy, the CEP90 ring at the mother centriole as observed by LR-ExSIM had
140 a smaller diameter (228 ± 23 nm) and was proximal to the distal appendages. Thus, CEP90
141 comprises a nine-fold ring at the distal centriole.
142
143 **CEP90, OFD1 and MNR form a distal centriole complex**
144 To gain insight into the function of CEP90 at the distal centriole, we proteomically identified
145 CEP90 interactors. More specifically, we generated RPE1 cell lines stably expressing GFP
146 (control) or YFP-CEP90. To discriminate proteins interacting with CEP90 at centriolar satellites
147 and those interacting with CEP90 at centrioles, we also generated *PCM1*$^{-/-}$ RPE1 cell lines stably
148 expressing GFP or YFP-CEP90 in which centriolar satellites are disrupted (Fig. 2a). We
149 immunoprecipitated GFP from these cell lines and detected co-immunoprecipitating proteins by
150 LC/MS/MS. Significance analysis of interactome (SAINTexpress (Teo et al., 2014)) analysis with
151 Bayesian false discovery rate (BFDR) < 0.05 indicated high confidence interactors (Fig. 2b and
152 c). Some CEP90 interactors, such as PCM1, CEP131 and BBS4, were identified in wild type cells,
153 but not in *PCM1*$^{-/-}$ cells, suggesting that these interactions are dependent on centriolar satellites.
154 Consistent with this conclusion, many of these PCM1-dependent interactors, including CEP131
155 and BBS4, are components of centriolar satellites (Hori and Toda, 2017).
156 To identify centriolar interactors of CEP90, we assessed which interactors were detected
157 in both WT and *PCM1*$^{-/-}$ RPE1 cells, as these interactions are predicted to be independent of
158 centriolar satellites. Notably, OFD1 and MNR, previously described components of centriolar
159 satellites and centrosomes that interact with each other (Chevrier et al., 2016), were detected as
160 CEP90 interactors (Fig. 2b and c). Using co-immunoprecipitation, we confirmed that CEP90
161 interacts with PCM1, MNR and OFD1 (Fig. 2d). Phylogenetic analysis revealed that CEP90, MNR
162 and OFD1 are largely co-conserved in metazoans, but absent in ecdysozoa such as *Drosophila*
163 *melanogaster* and *Caenorhabditis elegans* (Fig. 2e).
164 To assess whether MNR and OFD1 co-localize with CEP90, we immunostained RPE1
165 cells. CEP90 co-localized with MNR at centriolar satellites (Fig. 3a), and in cells treated with
166 nocodazole to disperse centriolar satellites, at centrioles (Fig. 3b). Similarly, MNR and OFD1 co-
167 localized at centriolar satellites (Fig. 3c), and centrioles in nocodazole treated cells (Fig. 3d). Thus,
168 like CEP90 and OFD1, MNR is a component of both centriolar satellites and centrioles.

169 To gain insight into the spatial organization of distal centriole proteins with respect to distal
170 appendages, we analyzed radially oriented centrioles with 3D-SIM (Fig. 3e). Consistent with
171 previous observations, distal appendage components CEP164 and CEP83 were organized into
172 respectively larger and smaller rings at the mother centriole (Yang et al., 2018; Bowler et al.,
173 2019). Of the distal centriole proteins, MNR was organized into the smallest ring (244 ± 29 nm)
174 (Fig. 3e and 3f). Talpid3, OFD1 and CEP90 also were organized into rings that, intriguingly, were
175 of different diameters at the mother and daughter centrioles. At the mother centriole, rings, from
176 largest to smallest, were comprised of Talpid3 (345 ± 27 nm), OFD1 (317 ± 37 nm) and CEP90
177 (291 ± 35 nm). At the daughter centriole, these rings were smaller and ordered differently from
178 largest to smallest as OFD1 (288 ± 21 nm), CEP90 (263 ± 21 nm) and Talpid3 (255 ± 24 nm) (Fig.
179 3e and 3f), indicating that the distal centriole is reorganized when the daughter centriole matures
180 into a mother.
181 Centriole biogenesis is coordinated with the cell cycle. Procentrioles form during S phase
182 and elongate in G2. To ascertain when distal centriole proteins are recruited to centrioles, we
183 used EdU incorporation and CENPF staining to distinguish between cells in different stages of
184 the cell cycle (Viol et al., 2020). CEP90, OFD1 and MNR localized to mother and daughter
185 centrioles in cells in G1 (EdU negative, CENPF negative) and in S phase (EdU positive, CENPF
186 negative) (Fig. 3g). In G2 (EdU negative, CENPF positive), both centrosomes (marked by γ-
187 tubulin) each possessed two puncta of CEP90, OFD1 and MNR (Fig. 3g). Therefore, CEP90,
188 OFD1 and MNR are recruited to the distal end of elongating procentrioles in G2.
189
190 **CEP90 and MNR are critical for vertebrate development, ciliogenesis and Hedgehog**
191 **signaling**
192 To assess the function of CEP90 and MNR, we generated RPE1 cell lines lacking CEP90
193 and MNR using CRISPR/Cas9. Immunoblot analyses confirmed loss of protein in the mutant cell
194 lines (Supplementary Fig 1 a-d). Notably, *CEP90*$^{-/-}$ and *MNR*$^{-/-}$ RPE1 cells possess centrioles but
195 both lacked cilia (Fig. 4a and 4b). As we previously identified a role for OFD1 in cilium assembly
196 (Singla et al., 2010; Hunkapiller et al., 2011), we conclude that the CEP90, MNR, OFD1 distal
197 centriole complex is essential for ciliogenesis.
198 To query the function of CEP90 and MNR in vertebrates, we obtained *Cep90* and *Mnr*
199 mutant mice from IMPC. The *Cep90* mutant mice (*Pibf1*$^{tm1.1\ (KOMP)Vlcg}$) contain a deletion of 7 exons,
200 and the *Mnr* mutant mice (*4933427D14Rik*$^{tm1\ (KOMP)Vlcg}$) contain a deletion of 10 exons.
201 Heterozygous *Cep90* and *Mnr* mice were viable and fertile, with no obvious phenotypes.
202 Homozygous *Cep90* and *Mnr* mice did not survive beyond embryonic day (E) 9.5. At E9.5, *Cep90*$^{-}$

203 $^{/-}$ and *Mnr*$^{-/-}$ embryos displayed pericardial edema (Fig. 4c) and unlooped, midline hearts. One key
204 role for primary cilia is in transducing extracellular signals including Hedgehog proteins, secreted
205 morphogens required for vertebrate development. As lack of Smoothened, a central component
206 of the Hedgehog signal transduction pathway, or lack of cilia also produces unlooped, midline
207 hearts (Corbit et al., 2005; Huangfu et al., 2003), we examined the presence of cilia in *Cep90*$^{-/-}$
208 and *Mnr*$^{-/-}$ embryos. γ-tubulin-positive centrioles were detected in both wild type and *Cep90*$^{-/-}$
209 embryonic nodes at E8.5, but cilia were absent from *Cep90*$^{-/-}$ nodes (Fig. 4d). Consistent with a
210 defect in ciliogenesis, *Cep90*$^{-/-}$ embryos also displayed attenuated expression of the Hedgehog
211 target gene, *Gli1*, indicating defects in Hedgehog signal transduction (Fig. 4e). Similarly, cilia
212 detected by ARL13B staining were absent in neural tube sections from E9.5 *Mnr*$^{-/-}$ embryos (Fig.
213 4f). Thus, CEP90 and MNR are both required for vertebrate development, ciliogenesis, and
214 Hedgehog signaling.

215 To identify regions in CEP90 required for cilium assembly, we tested whether CEP90
216 lacking either the N-terminus, C-terminus or central domain (Kim et al., 2012) could support
217 ciliogenesis in *CEP90*$^{-/-}$ RPE1 cells (Fig. 4g). Unlike expression of the full length CEP90 (FL-
218 CEP90), CEP90 lacking the N terminal (CEP90$^{363-757}$) or the C-terminal (CEP90$^{1-363}$) regions failed
219 to rescue ciliogenesis defects in *CEP90*$^{-/-}$ RPE1 cells (Fig. 4g-i). A construct of CEP90 lacking
220 residues required for interaction with PCM1 (CEP90$^{\Delta 271-363}$) localized to the centrosomal region,
221 and partially rescued ciliogenesis defects in *CEP90*$^{-/-}$ RPE1 cells (Fig 4g-i). These data support a
222 role for both N and C-terminal regions of CEP90 in ciliogenesis, further highlighting its function as
223 a critical centriolar scaffold.

224 We also examined whether disease-associated variants of CEP90 compromise its ability to
225 support cilia assembly or centriolar satellite localization. Previously, we identified a rare variant in
226 CEP90 (CEP90^{E89Q}) associated with microcephaly (Kodani et al., 2015). Surprisingly, this variant
227 of CEP90 displayed normal localization to centrioles and centriolar satellites (Fig. 4i), but failed to
228 support ciliogenesis in *CEP90*$^{-/-}$ RPE1 cells (Fig. 4h). We also assessed two mutant forms of
229 CEP90 (CEP90^{R405Q} and CEP90^{D637A}) implicated in Joubert syndrome (Wheway et al., 2015)
230 (Fig.4g). Interestingly, both Joubert associated variants of CEP90 perturbed centriolar satellite
231 morphology (Fig. 4i), and showed reduced ability to support ciliogenesis in *CEP90*$^{-/-}$ RPE1 (Fig.
232 4h). Thus, our data suggest that distinct human disease-associated mutations in *CEP90*
233 differentially compromise centriolar satellite morphogenesis and ciliogenesis.
234
235
236

237 **MNR, but not CEP90, restricts centriolar length**

238 Since distal centriole proteins OFD1, Talpid3 and C2CD3 control centriole length, we
239 analyzed *CEP90*$^{-/-}$ and *MNR*$^{-/-}$ centrioles labeled with Tubulin^{Ac} and distal centriole protein
240 CEP162 by 3D-SIM. Compared to control centrioles, centriole length was not altered in *CEP90*$^{-/-}$
241 cells. However, centriole length was highly variable in *MNR*$^{-/-}$ cells, with ~30% of *MNR*$^{-/-}$ cells
242 containing hyper-elongated centrioles (some of which were over a micron long, Fig 5. a-c). The
243 hyper-elongated centrioles in *MNR*$^{-/-}$ cells possessed the distal centriole component CEP162 at
244 one end, suggesting that proximal-distal polarity is maintained despite the elongation (Fig. 5 a).
245 Serial section transmission electron microscopy (TEM) analysis confirmed the presence of
246 elongated centrioles in *MNR*$^{-/-}$ RPE1 cells (Fig. 5 d-e). Therefore, MNR restrains centriole
247 lengthening (Fig. 5f).

248 The abnormal centriole morphology in *MNR*$^{-/-}$ cells is reminiscent of the phenotype we
249 previously observed in *OFD1* mutant cells (Singla et al., 2010). Therefore, we examined the
250 localization of OFD1 in *MNR*$^{-/-}$ RPE1 cells. OFD1 failed to localize to the centrioles in the absence
251 of MNR, but not CEP90 (Fig. 5 g-h). Overexpressed MNR localizes to microtubules (Chevrier et
252 al., 2016) and microtubule-associated MNR can sequester endogenous OFD1 (Supplementary
253 figure 2). Therefore, MNR is necessary and sufficient to recruit OFD1 (Fig. 5 g-h). FOPNL has
254 been shown to promote microtubule depolymerization (Feng et al., 2017; Srivastava and Panda,
255 2017). Interestingly, the centriolar localization of FOPNL was attenuated in *MNR*$^{-/-}$, but not *CEP90*
256 $^{-/-}$ cells (Fig. 5 i-j). Our data support a model where MNR recruits FOPNL and OFD1 to restrain
257 centriole length, with CEP90 being dispensable for centriole length control and dedicated to
258 ciliogenesis.

259

260 **CEP90 and MNR are required for the removal of CP110 and CEP97 from the mother**
261 **centriole at the initiation of ciliogenesis**

262 Ciliogenesis depends on a specialized protein transport machinery called intraflagellar
263 transport (IFT). We examined whether IFT88 localization to basal bodies depends on CEP90 or
264 MNR, and found that IFT88 was decreased at the mother centriole of both *CEP90*$^{-/-}$ and *MNR*$^{-/-}$
265 RPE1 cells (Fig. 6 a,b).

266 A critical early step in ciliogenesis is the removal from the distal mother centriole of two
267 proteins that can inhibit ciliogenesis, CP110 and CEP97. We tested whether CEP90 or MNR
268 function removal of CP110 and CEP97 by examining *CEP90*$^{-/-}$ and *MNR*$^{-/-}$ RPE1 cells. We found
269 that cells lacking either CEP90 or MNR fail to remove CP110 and CEP97 (Fig. 6 c-f). Taken
270 together, these results reveal that CEP90 and MNR are required for early steps of ciliogenesis.

271

272 **CEP90 and MNR are required for ciliary vesicle docking and distal appendage assembly**

273 Recent studies show that inhibitory daughter centriole proteins (such as CEP120 and
274 Centrobin) must be removed from the mother centriole to enable ciliogenesis (Wang et al., 2018;
275 Mahjoub et al., 2010). As removing daughter centriole proteins requires distal centriole proteins,
276 such as Talpid3, we examined the localization of Talpid3 and found that Talpid3 is recruited to
277 the distal centriole independently of CEP90 (Supplementary Fig 3a and b). Furthermore, daughter
278 centriole proteins are asymmetrically localized in *CEP90*$^{-/-}$ and *MNR*$^{-/-}$ RPE1 cells (Supplementary
279 Fig 3 c and d). Therefore, CEP90 and MNR regulate distal appendage formation through a
280 mechanism independent of Talpid3 recruitment or daughter centriole protein removal.

281 As ciliary vesicle formation contributes to removing CP110 and CEP97 from the mother
282 centriole (Westlake et al., 2011; Lu et al., 2015), we investigated whether persistence of CP110
283 and CEP97 in *CEP90*$^{-/-}$ and *MNR*$^{-/-}$ cells was due to defective recruitment of preciliary vesicles.

284 To assess whether CEP90 and MNR affect preciliary vesicle recruitment, we examined
285 the localization of Myosin-Va-positive preciliary vesicles (Wu et al., 2018) to centrioles in wild
286 type, *CEP90*$^{-/-}$ and *MNR*$^{-/-}$ RPE1 cells. Consistent with the defect in distal appendage formation,
287 cells lacking either CEP90 or MNR showed reduced Myosin-Va at the mother centriole (Fig. 6g-
288 h). To confirm the requirement for both CEP90 and MNR in preciliary vesicle recruitment, we
289 examined wild-type and knockout cells by serial section TEM, which confirmed that centrioles in
290 cells lacking CEP90 or MNR fail to dock to preciliary vesicles (Fig. 6i-j and Supplementary Figures
291 4 and 5). Thus, CEP90 and MNR are essential for ciliary vesicle recruitment to the mother
292 centriole, a key early step of ciliogenesis (Fig. 6k).

293 An early step of ciliogenesis is the acquisition of appendages by the mother centriole,
294 defining its maturation into a basal body. Sub-distal appendages mediate the anchoring of the
295 basal body to microtubules and regulate the spatial positioning of the cilium in the cell (Mazo et
296 al., 2016). In *CEP90*$^{-/-}$ and *MNR*$^{-/-}$ RPE1 cells, the localization of components of sub-distal
297 appendages, such as Ninein and CEP170, were unaffected (Supplementary Fig 6a-d), indicating
298 that CEP90 and MNR are dispensable for subdistal appendage formation.

299 A function of distal appendages is the recruitment of small preciliary vesicles to the mother
300 centriole which fuse and give rise to the ciliary membrane (Tanos et al., 2013; Schmidt et al.,
301 2012a). *CEP90*$^{-/-}$ and *MNR*$^{-/-}$ centrioles fail to recruit distal appendage proteins CEP83, FBF1,
302 SCLT1, ANKRD26 and CEP164, indicating that they are essential for distal appendage formation
303 (Fig. 7 c-g). CEP90 and MNR are not critical for distal appendage protein abundance

304 (Supplementary Fig 6e), suggesting that they are not required for distal appendage protein
305 stability but rather are essential for distal appendage assembly at the mother centriole.
306
307 **CEP90 functions at the mother centriole to support distal appendage formation**
308 Using siRNA-mediated gene knockdown, a previous study showed that CEP90 promotes
309 centriolar satellite accumulation in the vicinity of centrosomes. We confirmed that, in *CEP90*$^{-/-}$
310 RPE1 cells, PCM1- positive centriolar satellites failed to accumulate around centrosomes
311 (Supplementary Fig 7a and 7b). Interestingly, loss of MNR did not affect targeting of PCM1-
312 positive centriolar satellites to the centrosome (Supplementary Fig 7a and 7b), indicating that
313 CEP90 and MNR have some distinct functions in centriolar satellite distribution. These
314 observations raised the interesting possibility that CEP90-dependent targeting of centriolar
315 satellites to the centrosomal area promotes distal appendage formation and ciliogenesis.
316 As *PCM1*$^{-/-}$ cells lack centriolar satellites but retain CEP90 at centrioles (Fig. 1c), these
317 cells can help disentangle the functions of CEP90 and MNR at centriolar satellites and centrioles.
318 In accordance with previous observations (Wang et al., 2016; Odabasi et al., 2019), RPE1 cells
319 lacking PCM1 displayed compromised ciliogenesis (Supplementary Fig 7c). In stark contrast to
320 *CEP90*$^{-/-}$ cells, distal appendage components CEP83, SCLT1and CEP164 localized equivalently
321 to the mother centrioles of *PCM1*$^{-/-}$ and wild type RPE1 cells (Supplementary Fig 7d-i), indicating
322 that distal appendage assembly is independent of PCM1. Furthermore, serial section
323 transmission electron microscopy confirmed the presence of distal appendages in *PCM1*$^{-/-}$ RPE1
324 cells (Supplementary Fig 7j). As the critical centriolar satellite scaffold PCM1 is not required for
325 either CEP90 localization to centrioles or distal appendage formation, we conclude that the
326 centriolar satellite population of CEP90 is dispensable for distal appendage assembly.
327 If the centriolar satellite population is dispensable, we predicted that MNR and OFD1
328 recruitment of CEP90 to the distal centriole would be critical for distal appendage assembly and
329 ciliogenesis. Indeed, we found that CEP90 failed to localize to centrioles in *MNR*$^{-/-}$ RPE1 cells,
330 while MNR localized to the centrioles in the absence of CEP90 (Fig. 8 a-d).
331 To investigate how CEP90 can be specifically required for the formation distal
332 appendages, we investigated whether CEP90 interacts with the distal centriole base. Co-
333 immunoprecipitation analysis revealed an interaction between CEP90 and the proximal most-
334 component of the distal centriole, CEP83 (Fig. 8e). We propose that MNR recruits CEP90 to the
335 distal centriole, and CEP90, in turn, recruits CEP83 to initiate distal appendage assembly (Fig.
336 8f). Therefore, distal centriolar proteins are recruited in a hierarchical manner, with MNR recruiting
337 OFD1 to restrict centriole length, and CEP90 dedicated to distal appendage assembly.

338

339 **DISCUSSION**

340 **CEP90 and MNR are critical for distal appendage assembly and ciliogenesis**

341 Through the process of mitosis, vertebrate daughter cells each inherit two centrioles. Yet,
342 only the older, mother centriole templates a cilium. In no small part, this unique function of the
343 mother centriole depends on its distal appendages, acquired during the previous G2/M phase. In
344 this study, we identify a complex of CEP90, OFD1 and MNR as part of the distal centriole critical
345 for distal appendage formation and ciliogenesis.

346 Consequent to their role in distal appendage formation, CEP90 and MNR are also required
347 for subsequent events in ciliogenesis, including recruitment of the preciliary vesicles that give rise
348 to the ciliary membrane, and loading of IFT88 (Sillibourne et al., 2013; Tanos et al., 2013). Unlike
349 some other centriolar proteins, such as CEP120 (Tsai et al., 2019), CEP90 and MNR are
350 specifically required for distal appendage formation, but dispensable for subdistal appendage
351 formation, revealing that discrete mother centriolar complexes support distal and subdistal
352 appendage assembly.

353 In mice, we found that CEP90 and MNR are essential for embryonic development, and
354 particularly for heart looping and Hedgehog signaling. Primary cilia are required for Hedgehog
355 signal transduction in vertebrates. A central component of the Hedgehog pathway is the seven-
356 pass transmembrane protein, Smoothened (Smo). Interestingly, *Cep90, Mnr* and *Smo* mutants
357 arrested at similar points in embryonic development and displayed similar phenotypes,
358 emphasizing the importance of CEP90 and MNR in ciliary Hedgehog signaling.

359

360 **MNR recruits OFD1 to regulate centriole length**

361 CEP90 and MNR colocalize with their interactor OFD1 at the distal ends of centrioles. We
362 found that distal centriole proteins are recruited to the centriole in a hierarchical manner. MNR
363 forms the innermost ring at the distal centriole and is essential for the recruitment of OFD1 and
364 CEP90, whereas CEP90 is dispensable for the recruitment of the other complex members.
365 Overexpressed MNR localizes to microtubules (Chevrier et al., 2016) bringing along OFD1.
366 Therefore, we propose that MNR binds to the distal centriolar microtubules to recruit OFD1,
367 culminating in CEP90 recruitment (Fig. 8f).

368 We had previously demonstrated that OFD1 was essential to restrain centriolar length
369 (Singla et al., 2010). We have found that one of its partners, MNR, is also critical to restrict
370 centriolar elongation. However, its other partner, CEP90, does not control centriolar length. Thus,
371 within the complex comprised of MNR, OFD1 and CEP90, the subunits have distinct functions,

372 with CEP90 dedicated to founding distal appendages. Consequently, the requirement for MNR
373 and OFD1 in distal appendage assembly may be due to their roles in recruiting CEP90 to the
374 distal centriole.
375
376 **CEP90 recruits CEP83 to initiate distal appendage assembly at the mother centriole**
377 The functions of centriolar satellites, although intimately associated with centrosomes,
378 remain unclear (Odabasi et al., 2019; Prosser and Pelletier, 2020). CEP90 is a component of
379 centriolar satellites, where it interacts with PCM1, the major scaffolding protein of centriolar
380 satellites (Kim et al., 2012). Like CEP90, its interactors MNR and OFD1 are centriolar satellite
381 proteins. As loss of CEP90 disrupts the peri-centrosomal localization of centriolar satellites, we
382 initially hypothesized that centriolar satellites transport CEP90 to centrioles, or that CEP90 acts
383 at centriolar satellites to transport distal appendage components to the mother centriole. In *PCM1*$^{-}$
384 $^{/-}$ RPE1 cells, centriolar satellites are disrupted but CEP90 remains at the distal centriole,
385 indicating that satellites are dispensable for CEP90 localization at centrioles. Moreover, to our
386 surprise, we found that *PCM1*$^{-/-}$ RPE1 cells assemble distal appendages. Thus, centriolar
387 satellites (and CEP90 at centriolar satellites) are dispensable for distal appendage assembly,
388 indicating that CEP90 functions at the distal centriole to build distal appendages.
389 A combination of expansion and structured illumination super-resolution microscopy
390 revealed that CEP90 decorates the distal centriole in a discontinuous ring-like pattern with nine-
391 fold symmetry; this ring of CEP90 is proximal to and smaller than the ring of CEP164. At the
392 centriole, CEP90 interacts with and is critical for the recruitment of the distal appendage
393 component CEP83. As CEP83 is the root of the distal appendage (Tanos et al., 2013), CEP90 is
394 required to initiate distal appendage formation. In support of this conclusion, no distal appendage-
395 like structures were observable in serial section transmission electron micrographs of cells lacking
396 CEP90. These data raise the tantalizing possibility that the nine-fold ring of CEP90 at the distal
397 centriole templates the assembly of the distal appendages.
398 In addition to MNR, OFD1 and CEP90, Talpid3 and C2CD3 localize to the distal centriole
399 and are required for distal appendage formation (Singla et al., 2010; Thauvin-Robinet et al., 2014;
400 Ye et al., 2014; Wang et al., 2018). We did not identify C2CD3 or Talpid3 in our proteomic
401 analysis, suggesting that they might be part of a distinct, distal centriole complex (Tsai et al.,
402 2019). Talpid3 recruitment, and the subsequent removal of daughter centriole protein, Centrobin
403 occurs normally in *CEP90*$^{-/-}$ RPE1 cells. Therefore, CEP90 acts independently or downstream of
404 Talpid3 recruitment and daughter centriole protein removal to regulate distal appendage
405 assembly.

406 Mutations in *CEP90* cause Joubert syndrome (Kodani et al., 2015; Wheway et al., 2015;
407 Hebbar et al., 2018), while *OFD1* and *MNR* cause Orofaciodigital and Joubert syndrome (Singla
408 et al., 2010; Stephen et al., 2017; Chevrier et al., 2016; Coene et al., 2009). Joubert and
409 Orofaciodigital syndromes have partially overlapping clinical features. Ultrastructural studies have
410 identified a cogwheel-like structure at the distal domain of human centrioles (Paintrand et al.,
411 1992; Ibrahim et al., 2009), raising the possibility that CEP90, MNR and OFD1 may be
412 components of this structure. We propose that this distal centriolar complex both controls
413 centriolar length and builds distal appendages, and that inherited defects in this cogwheel that
414 compromise these critical functions attenuate ciliogenesis, Hedgehog signaling and embryonic
415 patterning, resulting in Joubert and Orofaciodigital syndromes.
416

417 **MATERIAL AND METHODS**

418 **Mouse lines**

419 *Cep90* (*Pibf1*$^{tm1.1(KOMP)Vlcg}$) and *Mnr* (*4933427D14Rik*$^{tm1.1(KOMP)Vlcg}$) mice, generated in a
420 C57BL/6NJ background were obtained from the International Mouse Phenotyping Consortium.
421 Mice were housed in a barrier facility with veterinary supervision and given food and water *ad*
422 *libitum*. All mouse protocols were approved by the Institutional Animal Care and Use Committee
423 at the University of California, San Francisco and the University of Alabama, Birmingham.

424 **Cell lines and cell culture**

425 Human retinal epithelial (RPE1-hTERT) cells were cultured in DMEM/F12 (Thermo Fisher;
426 catalog 10565042) supplemented with 10 % FBS at 37 ºC in 5% CO_2. To induce ciliation, cells
427 were serum starved in Opti-MEM reduced serum media for indicated times.

428 RPE1 cell lines stably expressing eYFP-CEP90 were generated using lentiviruses containing the
429 human *CEP90* cDNA (gift from Kunsoo Rhee (Kim and Rhee, 2011; Kim et al., 2012)) in the
430 pLVX-IRES-Puro (Clontech, Mountain View, CA) plasmid background. *CEP90*$^{-/-}$ RPE1 cells
431 expressing mNeonGreen-tagged full length, truncation and disease-associated mutation variants
432 of CEP90 were generated using lentiviruses containing human *CEP90* cDNA in a pLVX-EF1α$^{\Delta}$-
433 mNeonGreen plasmid background. Lentiviruses were generated using the Lenti-X Packaging
434 Single Shot system (Takara Bio), according to manufacturer's guidelines. Infected cells were
435 plated in a glass-bottom 96 well plate (Cellvis; catalog P96-1.5H-N) using limiting dilution and
436 monoclonal cell lines expressing eYFP-CEP90 were manually selected based on fluorescence.

437 RPE1 cells stably expressing HA-CEP83 under the control of tetracycline-inducible promoter were
438 a gift from Barbara Tanos and Bryan Tsou (Tanos et al., 2013). CEP83 expression was induced
439 with 1 µg/ml doxycycline (Fischer Chemical; Catalog BP26535) for 48 h.

440 All cell lines were routinely tested for mycoplasma contamination and found negative.

441 **Generation of *CEP90*$^{-/-}$, *MNR*$^{-/-}$ and *PCM1*$^{-/-}$ RPE1 cells by CRISPR/Cas9 gene targeting**

442 RNA guided targeting of *CEP90* and *MNR* was achieved by coexpression of Cas9 along with
443 guide RNAs. The pSpCas9 (BB)-2A-GFP (PX458) was a gift from Feng Zhang (Addgene plasmid
444 # 48138; http://n2t.net/addgene:48138 ; RRID:Addgene_48138). The gRNA sequences used for
445 CEP90 and MNR were 5′-GATGAGGAAATATCATCCGT-3′ and 5′-
446 GTATAAAATACCCGACCACA-3′ respectively.

447 *PCM1*$^{-/-}$ RPE1 cells were generated by electroporating recombinant Cas9 along with sgRNAs
448 (CRISPRevolution sgRNA EZ kit, Synthego). The sgRNA targeting exon 4 of human *PCM1*: 5′-
449 GAAAAGAAUAAGAAAAAGUU-3′ was used. 1.5 nmol sgRNA was resuspended in 15 µl
450 nuclease-free TE for a final concentration of 100 µM (100 pmol/µl). The RNP mixture containing
451 1.8 µl of sgRNA with 3 µl (90 pmol) Truecut Cas9 v2 (Thermo Fisher; catalog A36498) in a total
452 volume of 5 µl was incubated at room temperature for 15 minutes. The RNP mixture was
453 electroporated into hTERT-RPE1 cells using the Neon transfection system (Thermo Fisher)
454 according to manufacturer's instruction using the following parameters: 1350 V pulse voltage, 20
455 ms pulse width and 2 pulses. All electroporated cells were serially diluted, and single colonies
456 screened by western blotting, immunofluorescence and PCR analyses. For genotyping, the
457 following PCR primers were used: 5′-TGGGATGCACTAAATTGCCTA-3′ and 5′-
458 TTACCTGCCGTTTGAAGACA-3′ for *CEP90* alleles, 5′- TCCAGTGAACCAACTCACAGA-3′ and
459 5′-TAGGAGCGTGGCTGTGTCTAT -3′ for MNR alleles, and 5′- ACAGGCCATGTTAATTTTTGCT
460 -3′ and 5′- CCATCCCCAGTGATTAAAATTC -3′ for *PCM1* alleles. PCR products were cloned and
461 sequenced.

462 **Plasmids and transfections**

463 Myc-DDK tagged *Mnr* (*4933427D14Rik*) cDNA in cloned in a pCMV6 plasmid was obtained from
464 Origene (MR211309). hTERT-RPE1 cells were transfected using TransIT-LT1 transfection
465 reagent (Mirus Bio) according to manufacturer guidelines.

466

467

468 **Antibodies**

469 The list of primary antibodies and the dilution they were used at are listed in Supplementary Table
470 1. Secondary antibodies conjugated to Alexa Fluor 488, 568 and 647 were purchased from
471 Thermo Fisher Scientific, and used at a 1:500 dilution.

472 **Immunofluorescence**

473 For immunostaining, cells were fixed with either 100% cold methanol for 3 minutes or 4%
474 paraformaldehyde in dPBS for 15 minutes at room temperature, and then incubated in blocking
475 buffer (2.5% BSA, 0.1% Triton-X 100 in PBS) for 1 hour at room temperature. Paraformaldehyde
476 fixed cells were permeabilized with 0.1% Triton X-100 in PBS for 15 minutes at room temperature
477 prior to addition of blocking buffer. Coverslips were incubated with primary antibodies in blocking
478 buffer overnight at 4 °C, washed three times with PBS and incubated in secondary antibodies in
479 blocking buffer for 1-2 h at room temperature. Nuclei were counterstained with Hoechst 33352
480 (Thermo Fisher Scientific; catalog H3570). Coverslips were washed three times with PBS and
481 mounted with Prolong Diamond (Thermo Fisher Scientific; catalog P36961).

482 In experiments requiring disruption of the microtubule cytoskeleton, cells were treated with 20 μM
483 Nocodazole (Sigma Aldrich; catalog SML1665) for 2 h at 37 ºC prior to fixation.

484 Identification of cell cycle stages was performed as described previously (Viol et al., 2020), using
485 the Click-iT EdU Alexa Fluor 555 imaging kit (Life Technologies). Briefly, *PCM1*$^{-/-}$ RPE1 cells were
486 treated with 10 μM EdU for 30 minutes and fixed in 100% cold methanol for 3 minutes. The Click-
487 IT reaction was performed according to manufacturer guidelines, and samples subsequently
488 processed for indirect immunofluorescence. Cells lacking CENPF and EdU in the nucleus were
489 categorized as G1. EdU-positive, CENPF-negative cells were categorized as S, while cells with
490 nuclear CENPF staining, without EdU staining were classified as being in G2.

491 **Super-resolution microscopy**

492 3D-SIM and 2D-SIM was performed using the DeltaVision OMX-SR microscope (GE Healthcare)
493 using the 60x/1.42 NA oil immersion PSF objective and three sCMOS cameras. Immersion oil
494 with refractive index of 1.518 was used for most experiments. Z stacks of 5-6 μm were collected
495 using a 0.125 μm step size. Raw images were reconstructed using SoftWorx 6.5.2 (GE
496 Healthcare) using default parameters.

497 Label-retention expansion microscopy was performed as described previously (Shi et al., 2019).
498 Briefly, RPE1 cells were cultured on 16-well chambered slides (Sigma; catalog GBL112358-8EA)

499 coated with 0.1% gelatin (Sigma Aldrich; catalog G1393). Cells were serum starved in Opti-MEM
500 to induce ciliation for 24 h prior to fixation. After incubation with primary antibodies, cells were
501 incubated with appropriate secondary antibodies conjugated to NHS-MA-biotin or NHS-MA-DIG.
502 After gel polymerization and proteinase K digestion, gels were stained with fluorescently labeled
503 streptavidin or digitonin antibodies and images were acquired on the DeltaVision OMX-SR.

504 **Fluorescence intensity measurements and statistical analyses**

505 For fluorescence intensity measurements, z stacks were acquired on the DeltaVision OMX-SR
506 using widefield settings. Identical laser power and exposure settings were used for control and
507 experimental samples. Average intensity projections were generated using Image J (Schneider
508 et al., 2012), and images transferred to CellProfiler image analysis software (McQuin et al., 2018).
509 Cilia number were quantified by using Hoechst stained nuclei to count the total number of cells,
510 and a cilia marker (Arl13b/Tubulin^{Ac}) to identify cilia using the object identification module in
511 CellProfiler using difference in signal intensity and size to segment cilia. For quantification of
512 centrosomal intensity, a mask around the centrosomal area was generated using a centrosomal
513 marker (γ-tubulin/FOP) to identify the centrosome in CellProfiler. This centrosomal mask was
514 used to determine fluorescence intensity (integrated intensity) and area (in pixels) for the channel
515 of interest. Fluorescence intensity values in a pericentrosomal area were used to measure
516 background. Cells were serum starved for 24 h prior to fixing, to synchronize cells in G0/G1 and
517 eliminate cell cycle-dependent alterations in centrosomal proteins. Data were exported to
518 Microsoft Excel, and graphs generated in GraphPad Prism 8.

519 Statistical analyses were performed using GraphPad Prism 8. Results represented are mean ±
520 standard deviation. Statistical differences between data sets were analyzed using one-way Anova
521 with Tukey's multiple comparison tests or a two-tailed unpaired student's t test. P value < 0.05
522 was considered significant and indicated with an asterisk. NS denotes not significant.

523 **Transmission electron microscopy**

524 For electron microscopy, cells were plated on 8-well Permanox slides (Nunc; catalog177445),
525 gently washed in 0.1 M phosphate buffer (PB) and fixed in 3.5% EM-grade glutaraldehyde
526 (Electron Microscopy Sciences; catalog 16210) in 0.1M Phosphate buffer (PB) for 10 minutes at
527 37 ºC. Fixative was removed, replaced with fresh fixative, and samples incubated at 4 ºC for 1 h.
528 Slides were washed three times with 0.1 M PB and processed for TEM as described previously
529 (Singla et al., 2010).

530 **Co-immunoprecipitation and Western Blotting**

531 Cells grown in 10 cm petri dishes were washed twice with ice-cold dPBS and lysed for 30 minutes
532 on ice with frequent pipetting. Lysis buffer used was 10 mM Tris/Cl pH 7.5, 150 mM NaCl, 0.5 mM
533 EDTA, 0.5 % Nonidet P40 substitute supplemented with 1x protease inhibitor (Roche cOmplete
534 mini, EDTA free; catalog 4693159001) and 1x phosphatase inhibitor (Thermo Fisher PhosStop;
535 catalog 4906845001) cocktails. Lysates were cleared by centrifugation at 17,000 g for 10 minutes
536 at 4 ºC. GFP-trap magnetic agarose (Chromotek; catalog gtma-10) was used for eYFP-CEP90
537 co-immunoprecipitation assays, and HA-magnetic beads (Pierce; catalog 88837) for CEP83-HA
538 co-immunoprecipitation assays. Co-immunoprecipitation assays were performed according to
539 manufacturer guidelines. Samples were separated on 4-15% Criterion TGX Precast gels (Bio-
540 Rad), and transferred to Immobilon PVDF membranes (0.45 µm pore size) for
541 chemiluminescence detection.

542 **Mass spectrometry and data analysis**

543 Eluates obtained after co-immunoprecipitation were reduced by the addition of 1 mM DTT at 60°C
544 for 15 minutes, cooled to room temperature, alkylated by the addition of 3 mM iodoacetamide for
545 45 minutes in the dark. Alkylation was quenched by the addition of 3 mM DTT and proteins were
546 digested overnight at 37°C with 1 μg trypsin (0.5 μg/μl; Promega). Following digestion, peptides
547 were acidified with trifluoroacetic acid (0.5% final, pH < 2), desalted using UltraMicroSpin Columns
548 (PROTO 300 C18 300Å; The NEST Group) according to manufacturer's specifications, and dried
549 under vacuum centrifugation. Samples were resuspended in 4% formic acid, 4%
550 acetonitrile solution, and separated by an reversed-phase gradient over a nanoflow column (360
551 μm O.D. x 75 μm I.D.) packed with 25 cm of 1.8 μm Reprosil C18 particles with (Dr. Maisch). The
552 HPLC buffers were 0.1% formic acid and 100% acetonitrile on 0.1% formic acid for buffer A and
553 B respectively. The gradient was operated at 400 nL/min from 0 to 28% buffer B over 40min,
554 followed by a column wash at 95% B, with a total acquisition time of 50 min. Eluting peptides were
555 analyzed in on a Bruke timsTOF Pro mass spectrometry system equipped with a Bruker
556 nanoElute high-pressure liquid chromatography system interfaced via a captiveSpray source. A
557 data-dependent PASEF acquisition (Meier et al., 2018) method was used for data acquisition
558 using the following parameters: 100-1700 m/z range, 0.85-1.30 V*s/cm^2 trapped ion mobility
559 range, 1600V spray voltage, intensities of 200,000 were repeated for in PASEF 0 times, intensities
560 of 100,000 to 200,000 were repeated for in PASEF 5 times, intensities of less than 100,000 were
561 repeated for in PASEF 10 times, 4 PASEF MS/MS scans with a total cycle time of 0.53 s, and
562 active exclusion for 0.4 min. Data was search against the human proteome database (canonical
563 sequences downloaded from Uniprot 3/21/2018) using MaxQuant (Cox and Mann, 2008;

564 Prianichnikov et al., 2020). Peptide and protein identifications were filtered to 1% false-discovery
565 rate at the peptide and protein level, and protein-protein interaction analysis was performed using
566 SAINTexpress (Teo et al., 2014). The mass spectrometry data files (raw and search results) have
567 been deposited to the ProteomeXchange Consortium (Deutsch et al., 2017; Perez-Riverol et al.,
568 2019) (http://proteomecentral.proteomexchange.org) via the PRIDE partner repository with
569 dataset identifier PXD022372.

570 **ACKNOWLEDGEMENTS**

571 We thank E Yu for help with animal husbandry and genotyping of mice used in this study. We
572 thank members of the Reiter and Yoder labs for helpful discussions. This work was supported by
573 NIH R01HD089918 to J.F.R and B.Y., NIH R01R01DE029454 and R01AR054396 to J.F.R., the
574 Valencian Council for Innovation, Universities, Science and Digital Society
575 (PROMETEO/2019/075) to J.M.G-V and the Spanish Ministry of Science, Innovation and
576 Universities (PCI2018-093062) to V.H-P, NIH NIGMS R01GM124334 to B.H., by the NIH Pathway
577 to Independence Award K99GM126136/R00GM126136 and the UCSF Mary Anne Koda-Kimble
578 Seed Award for Innovation to X.S. D.K. is supported a Jane Coffin Childs Postdoctoral Fellowship,
579 and the Program for Breakthrough Biomedical Research Award, which is partially funded by the
580 Sandler Foundation. B. H. and J.F.R. are Chan Zuckerberg Biohub Investigators.

581

582 **FIGURE LEGENDS**

583 **Figure 1. CEP90 localizes to centriolar satellites and the distal centriole. a.** 3D-SIM of
584 immunostained RPE1 cells reveals localization of CEP90 (yellow) at centriolar satellites (PCM1,
585 cyan) and centrioles (Tubulin^{Ac}, magenta) in wild type RPE1 cells. Scale bar = 2 µm. **b**. Treatment
586 with nocodazole disperses the centriolar satellites, highlighting 3D-SIM of CEP90 (yellow) rings
587 at centrioles (γ-tubulin, magenta). Distal appendage component CEP164 (cyan) indicates the
588 mother centriole in C and D. Scale bar = 1 µm. **c**. 3D-SIM of *PCM1*$^{-/-}$ RPE1 cells shows that
589 CEP90 (yellow) localizes to centrioles (γ-tubulin, magenta) independent of centriolar satellites.
590 Scale bar = 1 µm. **d**. LR-ExSIM of RPE1 cells immunostained for CEP90 (yellow) and CEP164
591 (magenta) reveals that rings of CEP90 are comprised of discrete puncta. CEP90 rings are smaller
592 and more proximal to CEP164 rings. Scale bar = 1 µm. **e**. Schematic of the ring of CEP90 punctae
593 (yellow), distal appendages (magenta), and sub-distal appendages (blue) at the distal centriole.
594 CEP90 decorates the distal end of mother and daughter centrioles. **f**. Example of an LR-ExSIM
595 image of a radially oriented centriole used to quantify the number and angle between adjacent

596 puncta of CEP90. Scale bar = 0.5 μm. **g**. Histogram of number of discrete puncta of CEP90 and
597 CEP164 observed per centriole in LR-ExSIM images. **h**. Histogram of the angular spacing
598 between adjoining centriolar CEP90 puncta observed by LR-ExSIM.

599 **Figure 2. CEP90 forms a complex with OFD1 and MNR. a.** Schematic depicting workflow used
600 to identify CEP90 interactors at centriolar satellites and centrioles using WT and *PCM1*$^{-/-}$ RPE1
601 cells. *PCM1*$^{-/-}$ cells localize CEP90 to the distal centriole and WT cells localize CEP90 to the distal
602 centriole and centriolar satellites. **b**. Venn diagram comparing high confidence interactors of
603 CEP90 in WT and *PCM1*$^{-/-}$ RPE1 cells. **c**. Interactome dot representation of selected CEP90
604 interactors identified in the proteomic screen. Hits were grouped based on their cellular
605 localization. Average number of peptide spectra is represented by dot shade. Abundance of a
606 peptide spectrum produced in relation to the most abundant spectrum is depicted by dot size.
607 Bayesian false discovery rate (BFDR) is represented by rim color. **d**. Immunoblot of a subset of
608 CEP90 interactions identified by proteomics were validated by co-immunoprecipitation (IP).
609 CEP90 interacts with PCM1, OFD1 and MNR, but not α-tubulin or GAPDH. FT, flow through. **e.**
610 Coulson plot showing the phylogenetic distribution of a subset of centriolar proteins in select
611 ciliated metazoan species. Orthologs identified with high confidence are indicated with a filled
612 circle, and a subset of CEP90 interactors further explored in this study are highlighted in blue.The
613 dendrogram on top (made using iTOL (Ciccarelli et al., 2006)) shows the evolutionary relationship
614 between species.

615 **Figure 3. CEP90 co-localizes with OFD1 and MNR. a.** Immunostaining of RPE1 cells for CEP90
616 (yellow), MNR (cyan) and γ-tubulin (magenta) demonstrating that CEP90 co-localizes with MNR
617 at centriolar satellites. Scale bar = 2 μm. **b.** 3D-SIM of RPE1 cells treated with nocodazole to
618 disperse centriolar satellites highlights co-localization of CEP90 (yellow) and MNR (cyan) at
619 centrioles (γ-tubulin, magenta). Scale bar = 1 μm. **c**. Immunostaining of OFD1 (yellow), MNR
620 (cyan) and γ-tubulin (magenta) reveals CEP90 and MNR co-localization at centriolar satellites.
621 Scale bar = 2 μm. **d**. 3D-SIM of immunostained cells treated with nocodazole reveals a ring of
622 OFD1 (yellow) co-localizing with MNR (cyan) at centrioles (γ-tubulin, magenta). Scale bar =1 μm.
623 **e**. Measurements of ring diameters measured in 3D-SIM images. For distal centriole proteins, ring
624 diameters were measured at the mother (MC) and daughter centriole (DC). Scatter dot plot shows
625 mean ± SD. Asterisks indicate $p < 0.05$, and ns indicate not significant determined using unpaired
626 t test. **f**. Schematic representation of a radial view of a mother centriole with distal appendages
627 (purple), OFD1 (orange), CEP90 (yellow) and MNR (green). **g**. Localization of distal centriole
628 proteins (yellow) to centrioles (γ-tubulin, magenta) is cell cycle dependent. Cells in G1 were

629 identified as lacking both EdU and CENPF staining, cells in S as being positive for EdU but lacking
630 CENPF, and cells in G2 as being positive for CENPF but lacking EdU staining. Two puncta of
631 CEP90, OFD1 and MNR localized were observed at one centrosome during G1 and S, and four
632 puncta at two centrosomes after centrosome duplication during G2. Scale bar = 5 μm.

633 **Figure 4. CEP90 and MNR are essential for ciliogenesis. a**. WT, *CEP90*$^{-/-}$ and *MNR*$^{-/-}$ serum
634 starved RPE1 cells were immunostained for cilia (ARL13B, magenta), centrosomes (γ-tubulin,
635 yellow) and nuclei (Hoechst, blue). Scale bar = 10 μm. **b**. Quantification of ciliation frequency of
636 WT, *CEP90*$^{-/-}$ and *MNR*$^{-/-}$ RPE1 cells serum starved for times indicated. **c.** Images of control,
637 *Cep90*$^{-/-}$ and *Mnr*$^{-/-}$ embryos at embryonic day (E) 9.5. Arrows point to pericardial edema observed
638 in mutant embryos. **d**. Whole-mount immunostaining of nodes of littermate control and *Cep90*$^{-/-}$
639 embryos at E8.5 for centrosomes (γ-tubulin, yellow), cilia (Tubulin^{Ac}, magenta) and nuclei
640 (Hoechst, blue). Arrows in control image point to cilia projecting into the node lumen, which are
641 absent in *Cep90*$^{-/-}$ embryos. **e***. In situ* hybridization for *Gli1* in E8.5 littermate control and *Cep90*$^{-/-}$
642 embryos, revealing decreased expression in the absence of CEP90 indicative of disrupted
643 Hedgehog signaling. **f**. Immunostaining of E9.5 neural tube sections of littermate control and *Mnr*
644 $^{/-}$ embryos for centrosomes (FOP, yellow), cilia (ARL13B, magenta) and nuclei (Hoechst, blue),
645 indicating that MNR is required for ciliogenesis in vivo. Scale bar = 5 μm. **g**. Schematic
646 representation of full length (FL) human CEP90, truncation constructs and disease-associated
647 mutations. Coiled-coil (CC) domains identified by MARCOIL (Zimmermann et al., 2018) at 90%
648 threshold are indicated in cyan. **h**. Quantification of ciliation frequency of *CEP90*$^{-/-}$ RPE1 (control),
649 and *CEP90*$^{-/-}$ cells expressing mNeonGreen (mNG) tagged disease-variants and truncations of
650 CEP90. Graph shows mean ± SEM, and asterisks indicate $p < 0.05$ determined by one-way
651 ANOVA. **i**. *CEP90*$^{-/-}$ RPE1 cells, and *CEP90*$^{-/-}$ cells expressing the denoted mNG-tagged versions
652 of CEP90 were serum starved for 24 h and immunostained for cilia (ARL13B), centriolar satellites
653 (CEP131) and mNeonGreen. Scale bar = 2 μm.

654 **Figure 5. MNR, but not CEP90, restricts centriole length. a.** 3D-SIM images of WT, *CEP90*$^{-/-}$
655 and *MNR*$^{-/-}$ RPE1 cells immunostained for cilia (Tubulin^{Ac}, magenta) and CEP162 (yellow), a distal
656 centriolar protein. Scale bar = 1 μm. **b**. Graph of centriolar lengths measured using 3D-SIM
657 images. Centriole lengths are longer and have a wider distribution in *MNR*$^{-/-}$ cells than in WT or
658 *CEP90*$^{-/-}$ cells. Lines indicate mean ± SEM. Asterisks indicate $p < 0.05$ determined using one-way
659 ANOVA. **c**. Histogram of centriole lengths observed in WT, *MNR*$^{-/-}$ and *CEP90*$^{-/-}$ cells. **d**. Serial
660 section TEM confirms the presence of elongated centrioles in *MNR*$^{-/-}$ RPE1 cells. Scale bar = 500
661 nm. **e.** Centriole lengths of WT and *MNR*$^{-/-}$ RPE1 cells measured using TEM images. Horizontal

662 lines indicate means ± SEM, and asterisks indicate p<0.05 determined using unpaired t test. **f**.
663 Schematic depicting distinct roles of CEP90 and MNR in regulating centriole length. **g**. 3D-SIM
664 imaging of serum-starved WT, *CEP90*$^{-/-}$ and *MNR*$^{-/-}$ RPE1 cells immunostained for OFD1 (yellow),
665 centrioles (γ-tubulin, cyan) and cilia (Tubulin^{Ac}, magenta). Boxed regions are depicted in insets
666 throughout. OFD1 localizes to centrioles in WT and *CEP90*$^{-/-}$, but not *MNR*$^{-/-}$ cells. Scale bar = 1
667 µm. **h**. Quantification of OFD1 fluorescence intensity at centrioles in WT, *CEP90*$^{-/-}$ and *MNR*$^{-/-}$
668 cells. Horizontal lines indicate means ± SEM. Asterisks indicate p<0.05 determined using one-
669 way ANOVA.

670 **Figure 6. CEP90 and MNR are required for early ciliogenesis. a** WT, *CEP90*$^{-/-}$ and *MNR*$^{-/-}$
671 RPE1 cells immunostained for IFT88 (yellow), centrioles (γ-tubulin, cyan) and cilia (Tubulin^{Ac},
672 magenta. IFT88 is not recruited to the centrosome of *CEP90*$^{-/-}$ or *MNR*$^{-/-}$ cells. **b.** Quantification of
673 IFT88 fluorescence intensity at WT, *CEP90*$^{-/-}$ and *MNR*$^{-/-}$ centrosomes. **c**. WT, *CEP90*$^{-/-}$ and *MNR*
674 $^{-/-}$ serum-starved RPE1 cells immunostained for CP110 (yellow), centrioles (γ-tubulin, cyan) and
675 cilia (Tubulin^{Ac}, magenta). Scale bar = 1 µm. **d**. Quantification of whether CP110 localizes to one
676 or two centrioles. In the absence of CEP90 or MNR, CP110 continues to localize to the distal
677 mother centriole. Scale bar = 1 µm. **e**. WT, *CEP90*$^{-/-}$ and *MNR*$^{-/-}$ serum-starved RPE1 cells
678 immunostained for CEP97 (yellow), γ-tubulin (cyan) and Tubulin^{Ac} (magenta). Scale bar = 1 µm.
679 **f**. Quantification of whether CEP97 localizes to one or two centrioles. As with CP110, CEP90 and
680 MNR are required to remove CEP97 from the distal mother centriole. Scale bar = 1 µm. **g**. 3D-
681 SIM images of RPE1 cells immunostained for Myo-Va (yellow) and centrioles (γ-tubulin,
682 magenta). Myo-Va can not localize near centrosomes (left), can localize to preciliary vesicles
683 (denoted centrosomal Myo-Va, middle), or can localize to the ciliary pocket (denoted ciliary Myo-
684 Va, right). Scale bar = 1 µm. **h**. Quantification of three distinct Myo-Va staining patterns in WT,
685 *CEP90*$^{-/-}$ and *MNR*$^{-/-}$ cells. **i.** TEM images of serum-starved *Cep90*$^{+/+}$ and *Cep90*$^{-/-}$ MEFs confirms
686 the absence of preciliary vesicle docking at the *Cep90*$^{-/-}$ mother centriole. Scale bar = 200 nm. **j.**
687 TEM images of WT and *MNR*$^{-/-}$ RPE1 cells confirms the absence of preciliary vesicle vesicle
688 docking at the *MNR*$^{-/-}$ mother centriole. Scale bar = 250 nm. **k**. Model based on our data
689 highlighting the role of CEP90 and MNR in maturation of the mother centriole.

690 **Figure 7. CEP90 and MNR recruit distal appendage components to the mother centriole.**
691 3D-SIM images and quantification of centrosomal intensity of WT, *CEP90*$^{-/-}$ and *MNR*$^{-/-}$ RPE1 cells
692 immunostained for γ-tubulin (cyan), Tubulin^{Ac} (magenta) and distal centriole components (yellow)
693 CEP83 (**a,b**), FBF1 (**c,d**), SCLT1 (**e,f**), ANKRD26 (**g,h**) and CEP164 (**i,j**). Scale bar = 1 µm.

694 Horizontal lines in scatter dot plots indicate means ± SEM. Asterisks indicate p<0.001 determined
695 by one-way ANOVA.

696 **Figure 8. MNR recruits CEP90 which recruits CEP83 to build distal appendages. a.** 3D-SIM
697 imaging of WT, *CEP90*$^{-/-}$ and *MNR*$^{-/-}$ serum-starved RPE1 cells immunostained for CEP90
698 (yellow), γ-tubulin (cyan) and Tubulin^{Ac} (magenta). Scale bar = 1 μm. **b**. Quantification of CEP90
699 fluorescence intensity at centrioles. Horizontal lines in scatter dot plots indicate means ± SEM.
700 Asterisks indicate p < 0.0001, ns = not significant, determined using one-way ANOVA. CEP90
701 fails to localize to *MNR*$^{-/-}$ centrioles. **c**. 3D-SIM imaging of WT, *CEP90*$^{-/-}$ and *MNR*$^{-/-}$ serum-starved
702 RPE1 cells immunostained for MNR (yellow), γ-tubulin (cyan) and CEP164 (magenta). Scale bar
703 = 1 μm. **d.** Quantification of MNR fluorescence intensity at centrioles. Horizontal lines in scatter
704 dot plots indicate means ± SEM. Asterisks indicate p < 0.0001, determined using one-way
705 ANOVA. MNR localization is reduced but present at *CEP90*$^{-/-}$ centrioles. **e**. WT or RPE1 cells
706 expressing CEP83-HA were lysed, immunoprecipitated with anti-HA antibody bound beads and
707 immunoblotted with antibodies to HA and CEP90. **f**. Model of the hierarchical recruitment of distal
708 centriole proteins starting with MNR which recruits OFD1 to restrain centriole elongation and
709 CEP90 which recruits CEP83, the base of the distal appendage.

710

711 **SUPPLEMENTARY FIGURES:**

712 **SUPPLEMENTARY FIGURE 1. Generation of *CEP90*$^{-/-}$, *MNR*$^{-/-}$ and *PCM1*$^{-/-}$ cell lines.**
713 Sequence analysis of genomic DNA isolated from control and *CEP90*$^{-/-}$ (**a**), *MNR*$^{-/-}$ (**b**) and *PCM1*$^{-}$
714 $^{/-}$ (**c**) RPE1 cell lines generated using CRISPR-Cas9. Insertions and deletions, and translation
715 products resulting from genome editing are indicated. **d**. Immunoblot analysis of whole cell lysates
716 from control, *CEP90*$^{-/-}$, *MNR*$^{-/-}$ and *PCM1*$^{-/-}$ RPE1 cell lines confirms loss of protein in mutant cell
717 lines.

718 **SUPPLEMENTARY FIGURE 2. Overexpressed MNR localizes to microtubules and recruits**
719 **endogenous OFD1. a.** RPE1 cells transiently transfected with myc-tagged MNR and
720 immunostained with antibodies to myc-tag and α-tubulin. Scale bar = 10 μm. **b.** RPE1 cells
721 transiently transfected with myc-tagged MNR, and immunostained with antibodies to myc-tag and
722 OFD1. Scale bar = 10 μm. **c**. RPE1 cells transiently transfected with myc-tagged MNR, and
723 immunostained with antibodies to myc-tag and CEP90. Scale bar = 10 μm. **d**. RPE1 cells
724 transiently transfected with myc-tagged MNR, and immunostained with antibodies to myc-tag and
725 FOPNL. Scale bar = 10 μm.

726 **SUPPLEMENTARY FIGURE 3. CEP90 regulates distal appendage assembly independent**
727 **of Talpid3 recruitment and removal of Centrobin. a**. WT, *CEP90*$^{-/-}$ and *MNR*$^{-/-}$ RPE1 cells were
728 serum starved for 24 h and stained with antibodies to Talpid3, γ-tubulin (centrosome marker) and
729 Arl13b (cilia marker). 3D-SIM imaging reveals ring of Talpid3 at mother and daughter centrioles.
730 Scale bar = 1 μm. **b**. Quantification of Talpid3 fluorescence intensity at centrioles. Scatter dot
731 plots show mean ± SEM. Asterisks indicate p<0.001, determined using one-way ANOVA. **c**. WT,
732 *CEP90*$^{-/-}$ and *MNR*$^{-/-}$ serum-starved RPE1 cells immunostained for Centrobin (yellow), centrioles
733 (FOP, cyan) and distal appendages (CEP164, magenta). Scale bar = 1 μm. **d**. Quantification of
734 whether Centrobin localizes to one or two centrioles. CEP90 and MNR are not required to remove
735 Centrobin from the distal mother centriole.

736 **SUPPLEMENTARY FIGURE 4. Serial section TEM of WT and *Cep90*$^{-/-}$ MEF cells.** TEM images
737 of WT and *Cep90*$^{-/-}$ MEF cells confirms the absence of preciliary vesicle vesicle docking, and
738 distal appendages at the *Cep90*$^{-/-}$ mother centriole. Scale bar = 500 nm. Blue arrowheads indicate
739 subdistal appendages, and pink arrowheads indicate distal appendages. CP indicate ciliary
740 pocket.

741 **SUPPLEMENTARY FIGURE 5. Serial section TEM of WT and *MNR*$^{-/-}$ RPE1 cells.** TEM images
742 of WT and *MNR*$^{-/-}$ RPE1 cells confirms the absence of preciliary vesicle vesicle docking and distal
743 appendages at the *MNR*$^{-/-}$ mother centriole. Centrioles are hyper-elongated in the absence of
744 MNR. Scale bar = 500 nm. Blue arrowheads indicate subdistal appendages, and pink arrowheads
745 indicate distal appendages. CP indicate ciliary pocket.

746 **SUPPLEMENTARY FIGURE 6. CEP90 and MNR are dispensable for sub-distal appendage**
747 **assembly at the mother centriole. a.** 3D-SIM imaging of serum-starved WT, *CEP90*$^{-/-}$ and *MNR*$^{-}$
748 $^{/-}$ RPE1 cells immunostained for Ninein (yellow), centrioles (γ-tubulin, cyan) and cilia (ARL13B,
749 magenta). Boxed regions are depicted in insets throughout. Ninein localizes to centrioles in WT,
750 *CEP90*$^{-/-}$ and *MNR*$^{-/-}$ cells. Scale bar = 1 μm. **b**. Quantification of Ninein fluorescence intensity at
751 centrioles in WT, *CEP90*$^{-/-}$ and *MNR*$^{-/-}$ cells. Horizontal lines indicate means ± SEM. Asterisks
752 indicate p<0.05 determined using one-way ANOVA, ns indicates not significant. **c**. 3D-SIM
753 imaging of serum-starved WT, *CEP90*$^{-/-}$ and *MNR*$^{-/-}$ RPE1 cells immunostained for CEP170
754 (yellow), centrioles (γ-tubulin, cyan) and cilia (Tubulin^{Ac}, magenta). Boxed regions are depicted in
755 insets throughout. CEP170 localizes to centrioles in WT, *CEP90*$^{-/-}$ and *MNR*$^{-/-}$ cells. Scale bar = 1
756 μm. **b**. Quantification of CEP170 fluorescence intensity at centrioles in WT, *CEP90*$^{-/-}$ and *MNR*$^{-/-}$
757 cells. Horizontal lines indicate means ± SEM. Asterisks indicate p<0.05 determined using one-
758 way ANOVA.

759 **SUPPLEMENTARY FIGURE 7. Centriolar satellites are dispensable for distal appendage**
760 **assembly at the mother centriole. a.** 3D-SIM images of WT, *CEP90*$^{-/-}$ and *MNR*$^{-/-}$ RPE1 cells
761 immunostained with antibodies to PCM1, a centriolar satellite marker, Arl13b and γ-tubulin. Scale
762 bar = 2 μm. **b**. Quantification of PCM1 intensity in the pericentrosomal area. PCM1-positive
763 centriolar satellites fail to accumulate around centrosomes in *CEP90*$^{-/-}$, but not in *MNR*$^{-/-}$ cells. **c**.
764 Ciliogenesis is disrupted in *PCM1*$^{-/-}$ RPE1 cells at 24 h post serum starvation. **d**. WT and *PCM1*$^{-/-}$
765 RPE1 cells were serum starved for 24 h and stained with antibodies to CEP83, γ-tubulin
766 (centrosome marker) and Tubulin^{Ac} (cilia marker). 3D-SIM imaging reveals ring of CEP83 at the
767 mother centrioles in *PCM1*$^{-/-}$ RPE1 cells. Scale bar = 1 μm. **e**. Quantification of CEP83
768 fluorescence intensity at centrioles. Scatter dot plots show mean ± SEM. NS = not significant,
769 determined using one-way ANOVA. **f**. WT and *PCM1*$^{-/-}$ RPE1 cells were serum starved for 24 h
770 and stained with antibodies to SCLT1, γ-tubulin (centrosome marker) and Arl13b (cilia marker).
771 3D-SIM imaging reveals ring of SCLT1 at the mother centrioles in WT and *PCM1*$^{-/-}$ RPE1 cells.
772 Scale bar = 1 μm. **g**. Quantification of SCLT1 fluorescence intensity at centrioles. Scatter dot plots
773 show mean ± SEM. NS = not significant, determined using one-way ANOVA. **h**. WT and *PCM1*$^{-/-}$
774 RPE1 cells were serum starved for 24 h and stained with antibodies to CEP164 and γ-tubulin
775 (centrosome marker). 3D-SIM imaging reveals ring of CEP164 at the mother centrioles in *PCM1*$^{-}$
776 $^{/-}$ RPE1 cells. Scale bar = 1 μm. **i**. Quantification of CEP164 fluorescence intensity at centrioles.
777 Scatter dot plots show mean ± SEM. Asterisks indicate $p < 0.001$, determined using one-way
778 ANOVA. **j**. Representative TEM images of WT and *PCM1*$^{-/-}$ RPE1 cells serum starved for 1 hour.
779 Distal appendages are marked with red arrows.

780 **REFERENCES**

781 Andersen, J.S., C.J. Wilkinson, T. Mayor, P. Mortensen, E.A. Nigg, and M. Mann. 2003.
782 Proteomic characterization of the human centrosome by protein correlation profiling.
783 *Nature*. 426:570–574. doi:10.1038/nature02166.

784 Bowler, M., D. Kong, S. Sun, R. Nanjundappa, L. Evans, V. Farmer, A. Holland, M.R. Mahjoub,
785 H. Sui, and J. Loncarek. 2019. High-resolution characterization of centriole distal
786 appendage morphology and dynamics by correlative STORM and electron microscopy.
787 *Nat. Commun.* 10. doi:10.1038/s41467-018-08216-4.

788 Breslow, D.K., and A.J. Holland. 2019. Mechanism and Regulation of Centriole and Cilium
789 Biogenesis. *Annu. Rev. Biochem.* 88:691–724. doi:10.1146/annurev-biochem-013118-
790 111153.

791 Chevrier, V., A.-L. Bruel, T.J.P. Van Dam, B. Franco, M. Lo Scalzo, F. Lembo, S. Audebert, E.
792 Baudelet, D. Isnardon, A. Bole, J.-P. Borg, P. Kuentz, J. Thevenon, L. Burglen, L. Faivre,
793 J.-B. Rivière, M.A. Huynen, D. Birnbaum, O. Rosnet, and C. Thauvin-Robinet. 2016.
794 OFIP/KIAA0753 forms a complex with OFD1 and FOR20 at pericentriolar satellites and
795 centrosomes and is mutated in one individual with oral-facial-digital syndrome. *Hum. Mol.*
796 *Genet.* 25:497–513. doi:10.1093/hmg/ddv488.

797 Chong, W.M., W.-J. Wang, C.-H. Lo, T.-Y. Chiu, T.-J. Chang, Y.-P. Liu, B. Tanos, G. Mazo, M.-
798 F.B. Tsou, W.-N. Jane, T.T. Yang, and J.-C. Liao. 2020. Super-resolution microscopy
799 reveals coupling between mammalian centriole subdistal appendages and distal
800 appendages. *Elife*. 9. doi:10.7554/elife.53580.

801 Ciccarelli, F.D., T. Doerks, C. Von Mering, C.J. Creevey, B. Snel, and P. Bork. 2006. Toward
802 automatic reconstruction of a highly resolved tree of life. *Science (80-.).* 311:1283–1287.
803 doi:10.1126/science.1123061.

804 Coene, K.L.M., R. Roepman, D. Doherty, B. Afroze, H.Y. Kroes, S.J.F. Letteboer, L.H. Ngu, B.
805 Budny, E. van Wijk, N.T. Gorden, M. Azhimi, C. Thauvin-Robinet, J.A. Veltman, M. Boink,
806 T. Kleefstra, F.P.M. Cremers, H. van Bokhoven, and A.P.M. de Brouwer. 2009. OFD1 Is
807 Mutated in X-Linked Joubert Syndrome and Interacts with LCA5-Encoded Lebercilin. *Am.*
808 *J. Hum. Genet.* 85:465–481. doi:10.1016/j.ajhg.2009.09.002.

809 Corbit, K.C., P. Aanstad, V. Singla, A.R. Norman, D.Y.R. Stainier, and J.F. Reiter. 2005.
810 Vertebrate Smoothened functions at the primary cilium. *Nature*. 437:1018–1021.
811 doi:10.1038/nature04117.

812 Cox, J., and M. Mann. 2008. MaxQuant enables high peptide identification rates, individualized
813 p.p.b.-range mass accuracies and proteome-wide protein quantification. *Nat. Biotechnol.*
814 26:1367–1372. doi:10.1038/nbt.1511.

815 Deutsch, E.W., A. Csordas, Z. Sun, A. Jarnuczak, Y. Perez-Riverol, T. Ternent, D.S. Campbell,
816 M. Bernal-Llinares, S. Okuda, S. Kawano, R.L. Moritz, J.J. Carver, M. Wang, Y. Ishihama,
817 N. Bandeira, H. Hermjakob, and J.A. Vizcaíno. 2017. The ProteomeXchange consortium in
818 2017: Supporting the cultural change in proteomics public data deposition. *Nucleic Acids*
819 *Res.* 45:D1100–D1106. doi:10.1093/nar/gkw936.

820 Feng, S., Y. Song, M. Shen, S. Xie, W. Li, Y. Lu, Y. Yang, G. Ou, J. Zhou, F. Wang, W. Liu, X.
821 Yan, X. Liang, and T. Zhou. 2017. Microtubule-binding protein FOR20 promotes

822 microtubule depolymerization and cell migration. *Cell Discov.* 3:1–13.
823 doi:10.1038/celldisc.2017.32.

824 Goehring, N.W., and A.A. Hyman. 2012. Organelle growth control through limiting pools of
825 cytoplasmic components. *Curr. Biol.* 22:R330–R339. doi:10.1016/j.cub.2012.03.046.

826 Gönczy, P. 2015. Centrosomes and cancer: Revisiting a long-standing relationship. *Nat. Rev.*
827 *Cancer*. 15:639–652. doi:10.1038/nrc3995.

828 Hammarsjö, A., Z. Wang, R. Vaz, F. Taylan, M. Sedghi, K.M. Girisha, D. Chitayat, K.
829 Neethukrishna, P. Shannon, R. Godoy, K. Gowrishankar, A. Lindstrand, J. Nasiri, M.
830 Baktashian, P.T. Newton, L. Guo, W. Hofmeister, M. Pettersson, A.S. Chagin, G.
831 Nishimura, L. Yan, N. Matsumoto, A. Nordgren, N. Miyake, G. Grigelioniene, and S.
832 Ikegawa. 2017. Novel KIAA0753 mutations extend the phenotype of skeletal ciliopathies.
833 *Sci. Rep.* 7. doi:10.1038/s41598-017-15442-1.

834 Hebbar, M., A. Kanthi, A. Shukla, S. Bielas, and K.M. Girisha. 2018. A biallelic 36-bp insertion in
835 PIBF1 is associated with Joubert syndrome. *J. Hum. Genet.* 63:935–939.
836 doi:10.1038/s10038-018-0462-7.

837 Hori, A., and T. Toda. 2017. Regulation of centriolar satellite integrity and its physiology. *Cell.*
838 *Mol. Life Sci.* 74:213–229. doi:10.1007/s00018-016-2315-x.

839 Huangfu, D., A. Liu, A.S. Rakeman, N.S. Murcia, L. Niswander, and K. V. Anderson. 2003.
840 Hedgehog signalling in the mouse requires intraflagellar transport proteins. *Nature*.
841 426:83–87. doi:10.1038/nature02061.

842 Hunkapiller, J., V. Singla, A. Seol, and J.F. Reiter. 2011. The ciliogenic protein oral-facial-digital
843 1 regulates the neuronal differentiation of embryonic stem cells. *Stem Cells Dev.* 20:831–
844 841. doi:10.1089/scd.2010.0362.

845 Ibrahim, R., C. Messaoudi, F.J. Chichon, C. Celati, and S. Marco. 2009. Electron tomography
846 study of isolated human centrioles. *Microsc. Res. Tech.* 72:42–48. doi:10.1002/jemt.20637.

847 Jakobsen, L., K. Vanselow, M. Skogs, Y. Toyoda, E. Lundberg, I. Poser, L.G. Falkenby, M.
848 Bennetzen, J. Westendorf, E.A. Nigg, M. Uhlen, A.A. Hyman, and J.S. Andersen. 2011.
849 Novel asymmetrically localizing components of human centrosomes identified by
850 complementary proteomics methods. *EMBO J.* 30:1520–1535. doi:10.1038/emboj.2011.63.

851 Keller, L.C., S. Geimer, E. Romijn, J. Yates, I. Zamora, and W.F. Marshall. 2009. Molecular

852 architecture of the centriole proteome: The conserved WD40 domain protein POC1 is
853 required for centriole duplication and length control. *Mol. Biol. Cell*. 20:1150–1166.
854 doi:10.1091/mbc.E08-06-0619.

855 Keller, L.C., E.P. Romijn, I. Zamora, J.R. Yates, and W.F. Marshall. 2005. Proteomic analysis of
856 isolated Chlamydomonas centrioles reveals orthologs of ciliary-disease genes. *Curr. Biol.*
857 15:1090–1098. doi:10.1016/j.cub.2005.05.024.

858 Kim, K., K. Lee, and K. Rhee. 2012. CEP90 Is Required for the Assembly and Centrosomal
859 Accumulation of Centriolar Satellites, Which Is Essential for Primary Cilia Formation. *PLoS*
860 *One*. 7:e48196. doi:10.1371/journal.pone.0048196.

861 Kim, K., and K. Rhee. 2011. The pericentriolar satellite protein CEP90 is crucial for integrity of
862 the mitotic spindle pole. *J. Cell Sci.* 124:338–347. doi:10.1242/jcs.078329.

863 Kodani, A., T.W. Yu, J.R. Johnson, D. Jayaraman, T.L. Johnson, L. Al-Gazali, L. Sztriha, J.N.
864 Partlow, H. Kim, A.L. Krup, A. Dammermann, N.J. Krogan, C.A. Walsh, and J.F. Reiter.
865 2015. Centriolar satellites assemble centrosomal microcephaly proteins to recruit CDK2
866 and promote centriole duplication. *Elife*. 4:e07519. doi:10.7554/eLife.07519.

867 Kong, D., N. Sahabandu, C. Sullenberger, A. Vásquez-Limeta, D. Luvsanjav, K. Lukasik, and J.
868 Loncarek. 2020. Prolonged mitosis results in structurally aberrant and over-elongated
869 centrioles. *J. Cell Biol.* 219. doi:10.1083/jcb.201910019.

870 Lu, Q., C. Insinna, C. Ott, J. Stauffer, P.A. Pintado, J. Rahajeng, U. Baxa, V. Walia, A. Cuenca,
871 Y.S. Hwang, I.O. Daar, S. Lopes, J. Lippincott-Schwartz, P.K. Jackson, S. Caplan, and C.J.
872 Westlake. 2015. Early steps in primary cilium assembly require EHD1/EHD3-dependent
873 ciliary vesicle formation. *Nat. Cell Biol.* 17:228–240. doi:10.1038/ncb3109.

874 Mahjoub, M.R., Z. Xie, and T. Stearns. 2010. Cep120 is asymmetrically localized to the
875 daughter centriole and is essential for centriole assembly. *J. Cell Biol.* 191:331–346.
876 doi:10.1083/jcb.201003009.

877 Marteil, G., A. Guerrero, A.F. Vieira, B.P. De Almeida, P. Machado, S. Mendonça, M. Mesquita,
878 B. Villarreal, I. Fonseca, M.E. Francia, K. Dores, N.P. Martins, S.C. Jana, E.M. Tranfield,
879 N.L. Barbosa-Morais, J. Paredes, D. Pellman, S.A. Godinho, and M. Bettencourt-Dias.
880 2018. Over-elongation of centrioles in cancer promotes centriole amplification and
881 chromosome missegregation. *Nat. Commun.* 9:1–17. doi:10.1038/s41467-018-03641-x.

882 Mazo, G., N. Soplop, W.-J. Wang, K. Uryu, and M.-F. Bryan Tsou. 2016. Spatial Control of
883 Primary Ciliogenesis by Subdistal Appendages Alters Sensation-Associated Properties of
884 Cilia Developmental Cell Spatial Control of Primary Ciliogenesis by Subdistal Appendages
885 Alters Sensation-Associated Properties of Cilia. *Dev. Cell*. 39:424–437.
886 doi:10.1016/j.devcel.2016.10.006.

887 McQuin, C., A. Goodman, V. Chernyshev, L. Kamentsky, B.A. Cimini, K.W. Karhohs, M. Doan,
888 L. Ding, S.M. Rafelski, D. Thirstrup, W. Wiegraebe, S. Singh, T. Becker, J.C. Caicedo, and
889 A.E. Carpenter. 2018. CellProfiler 3.0: Next-generation image processing for biology.
890 *PLOS Biol.* 16:e2005970. doi:10.1371/JOURNAL.PBIO.2005970.

891 Meier, F., A.D. Brunner, S. Koch, H. Koch, M. Lubeck, M. Krause, N. Goedecke, J. Decker, T.
892 Kosinski, M.A. Park, N. Bache, O. Hoerning, J. Cox, O. Räther, and M. Mann. 2018. Online
893 parallel accumulation–serial fragmentation (PASEF) with a novel trapped ion mobility mass
894 spectrometer. *Mol. Cell. Proteomics*. 17:2534–2545. doi:10.1074/mcp.TIR118.000900.

895 Nigg, E.A., and A.J. Holland. 2018. Once and only once: Mechanisms of centriole duplication
896 and their deregulation in diseases. *Nat. Rev. Mol. Cell Biol.* 19:297–312.
897 doi:10.1038/nrm.2017.127.

898 Odabasi, E., S. Gul, I.H. Kavakli, and E.N. Firat-Karalar. 2019. Centriolar satellites are required
899 for efficient ciliogenesis and ciliary content regulation. *EMBO Rep.* 20.
900 doi:10.15252/embr.201947723.

901 Paintrand, M., M. Moudjou, H. Delacroix, and M. Bornens. 1992. Centrosome organization and
902 centriole architecture: Their sensitivity to divalent cations. *J. Struct. Biol.* 108:107–128.
903 doi:10.1016/1047-8477(92)90011-X.

904 Perez-Riverol, Y., A. Csordas, J. Bai, M. Bernal-Llinares, S. Hewapathirana, D.J. Kundu, A.
905 Inuganti, J. Griss, G. Mayer, M. Eisenacher, E. Pérez, J. Uszkoreit, J. Pfeuffer, T.
906 Sachsenberg, Ş. Yilmaz, S. Tiwary, J. Cox, E. Audain, M. Walzer, A.F. Jarnuczak, T.
907 Ternent, A. Brazma, and J.A. Vizcaíno. 2019. The PRIDE database and related tools and
908 resources in 2019: Improving support for quantification data. *Nucleic Acids Res.* 47:D442–
909 D450. doi:10.1093/nar/gky1106.

910 Prianichnikov, N., H. Koch, S. Koch, M. Lubeck, R. Heilig, S. Brehmer, R. Fischer, and J. Cox.
911 2020. Maxquant software for ion mobility enhanced shotgun proteomics. *Mol. Cell.*
912 *Proteomics*. 19:1058–1069. doi:10.1074/mcp.TIR119.001720.

913 Prosser, S.L., and L. Pelletier. 2020. Centriolar satellite biogenesis and function in vertebrate
914 cells. *J. Cell Sci.* 133. doi:10.1242/jcs.239566.

915 Reiter, J.F., and M.R. Leroux. 2017. Genes and molecular pathways underpinning ciliopathies.
916 *Nat. Rev. Mol. Cell Biol.* 18:533–547. doi:10.1038/nrm.2017.60.

917 Schmidt, K.N., S. Kuhns, A. Neuner, B. Hub, H. Zentgraf, and G. Pereira. 2012a. Cep164
918 mediates vesicular docking to the mother centriole during early steps of ciliogenesis. *J. Cell*
919 *Biol.* 199:1083–1101. doi:10.1083/jcb.201202126.

920 Schmidt, K.N., S. Kuhns, A. Neuner, B. Hub, H. Zentgraf, and G. Pereira. 2012b. Cep164
921 mediates vesicular docking to the mother centriole during early steps of ciliogenesis. *J. Cell*
922 *Biol.* 199:1083–1101. doi:10.1083/jcb.201202126.

923 Schneider, C.A., W.S. Rasband, and K.W. Eliceiri. 2012. NIH Image to ImageJ: 25 years of
924 image analysis. *Nat. Methods*. 9:671–675. doi:10.1038/nmeth.2089.

925 Shen, Y., H. Wang, Z. Liu, M. Luo, S. Ma, C. Lu, Z. Cao, Y. Yu, R. Cai, C. Chen, Q. Li, H. Gao,
926 Y. Peng, B. Xu, and X. Ma. 2020. Identification of two novel pathogenic variants of PIBF1
927 by whole exome sequencing in a 2-year-old boy with Joubert syndrome. *BMC Med. Genet.*
928 21:192. doi:10.1186/s12881-020-01130-x.

929 Shi, X., G. Garcia, J.C. Van De Weghe, R. McGorty, G.J. Pazour, D. Doherty, B. Huang, and
930 J.F. Reiter. 2017. Super-resolution microscopy reveals that disruption of ciliary transition-
931 zone architecture causes Joubert syndrome. *Nat. Cell Biol.* 19:1178–1188.
932 doi:10.1038/ncb3599.

933 Shi, X., Q. Li, Z. Dai, A. Tran, S. Feng, A.D. Ramirez, Z. Lin, X. Wang, T.T. Chow, I.B. Seiple,
934 and B. Huang. 2019. Label-retention expansion microscopy. *bioRxiv*. 687954.
935 doi:10.1101/687954.

936 Sillibourne, J.E., I. Hurbain, T. Grand-Perret, B. Goud, P. Tran, and M. Bornens. 2013. Primary
937 ciliogenesis requires the distal appendage component Cep123. *Biol. Open*. 2:535–545.
938 doi:10.1242/bio.20134457.

939 Singla, V., M. Romaguera-Ros, J.M. Garcia-Verdugo, and J.F. Reiter. 2010. Ofd1, a Human
940 Disease Gene, Regulates the Length and Distal Structure of Centrioles. *Dev. Cell*. 18:410–
941 424. doi:10.1016/j.devcel.2009.12.022.

942 Srivastava, S., and D. Panda. 2017. A centrosomal protein FOR20 regulates microtubule

943 assembly dynamics and plays a role in cell migration. *Biochem. J.* 474:2841–2859.
944 doi:10.1042/BCJ20170303.

945 Stephen, J., T. Vilboux, L. Mian, C. Kuptanon, C.M. Sinclair, D. Yildirimli, D.M. Maynard, J.
946 Bryant, R. Fischer, M. Vemulapalli, J.C. Mullikin, M. Huizing, W.A. Gahl, M.C. V. Malicdan,
947 and M. Gunay-Aygun. 2017. Mutations in KIAA0753 cause Joubert syndrome associated
948 with growth hormone deficiency. *Hum. Genet.* 136:399–408. doi:10.1007/s00439-017-
949 1765-z.

950 Tanos, B.E., H.J. Yang, R. Soni, W.J. Wang, F.P. Macaluso, J.M. Asara, and M.F.B. Tsou.
951 2013. Centriole distal appendages promote membrane docking, leading to cilia initiation.
952 *Genes Dev.* 27:163–168. doi:10.1101/gad.207043.112.

953 Teo, G., G. Liu, J. Zhang, A.I. Nesvizhskii, A.C. Gingras, and H. Choi. 2014. SAINTexpress:
954 Improvements and additional features in Significance Analysis of INTeractome software. *J.*
955 *Proteomics*. 100:37–43. doi:10.1016/j.jprot.2013.10.023.

956 Thauvin-Robinet, C., J.S. Lee, E. Lopez, V. Herranz-Pérez, T. Shida, B. Franco, L. Jego, F. Ye,
957 L. Pasquier, P. Loget, N. Gigot, B. Aral, C.A.M. Lopes, J. St-Onge, A.L. Bruel, J. Thevenon,
958 S. González-Granero, C. Alby, A. Munnich, M. Vekemans, F. Huet, A.M. Fry, S. Saunier,
959 J.B. Rivière, T. Attié-Bitach, J.M. Garcia-Verdugo, L. Faivre, A. Mégarbané, and M. V.
960 Nachury. 2014. The oral-facial-digital syndrome gene C2CD3 encodes a positive regulator
961 of centriole elongation. *Nat. Genet.* 46:905–911. doi:10.1038/ng.3031.

962 Tsai, J.J., W. Bin Hsu, J.H. Liu, C.W. Chang, and T.K. Tang. 2019. CEP120 interacts with
963 C2CD3 and Talpid3 and is required for centriole appendage assembly and ciliogenesis.
964 *Sci. Rep.* 9:1–15. doi:10.1038/s41598-019-42577-0.

965 Viol, L., S. Hata, A. Pastor-Peidro, A. Neuner, F. Murke, P. Wuchter, A.D. Ho, B. Giebel, and G.
966 Pereira. 2020. Nek2 kinase displaces distal appendages from the mother centriole prior to
967 mitosis. *J. Cell Biol.* 219. doi:10.1083/jcb.201907136.

968 Wang, L., M. Failler, W. Fu, and B.D. Dynlacht. 2018. A distal centriolar protein network controls
969 organelle maturation and asymmetry. *Nat. Commun.* 9. doi:10.1038/s41467-018-06286-y.

970 Wang, L., K. Lee, R. Malonis, I. Sanchez, and B.D. Dynlacht. 2016. Tethering of an E3 ligase by
971 PCM1 regulates the abundance of centrosomal KIAA0586/Talpid3 and promotes
972 ciliogenesis. *Elife*. 5. doi:10.7554/eLife.12950.

973 Wassie, A.T., Y. Zhao, and E.S. Boyden. 2019. Expansion microscopy: principles and uses in
974 biological research. *Nat. Methods*. 16:33–41. doi:10.1038/s41592-018-0219-4.

975 Westlake, C.J., L.M. Baye, M. V. Nachury, K.J. Wright, K.E. Ervin, L. Phu, C. Chalouni, J.S.
976 Beck, D.S. Kirkpatrick, D.C. Slusarski, V.C. Sheffield, R.H. Scheller, and P.K. Jackson.
977 2011. Primary cilia membrane assembly is initiated by Rab11 and transport protein particle
978 II (TRAPPII) complex-dependent trafficking of Rabin8 to the centrosome. *Proc. Natl. Acad.*
979 *Sci. U. S. A.* 108:2759–2764. doi:10.1073/pnas.1018823108.

980 Wheway, G., M. Schmidts, D.A. Mans, K. Szymanska, T.-M.T. Nguyen, H. Racher, I.G. Phelps,
981 G. Toedt, J. Kennedy, K.A. Wunderlich, N. Sorusch, Z.A. Abdelhamed, S. Natarajan, W.
982 Herridge, J. van Reeuwijk, N. Horn, K. Boldt, D.A. Parry, S.J.F. Letteboer, S. Roosing, M.
983 Adams, S.M. Bell, J. Bond, J. Higgins, E.E. Morrison, D.C. Tomlinson, G.G. Slaats, T.J.P.
984 van Dam, L. Huang, K. Kessler, A. Giessl, C. V. Logan, E.A. Boyle, J. Shendure, S. Anazi,
985 M. Aldahmesh, S. Al Hazzaa, R.A. Hegele, C. Ober, P. Frosk, A.A. Mhanni, B.N.
986 Chodirker, A.E. Chudley, R. Lamont, F.P. Bernier, C.L. Beaulieu, P. Gordon, R.T. Pon, C.
987 Donahue, A.J. Barkovich, L. Wolf, C. Toomes, C.T. Thiel, K.M. Boycott, M. McKibbin, C.F.
988 Inglehearn, F. Stewart, H. Omran, M.A. Huynen, P.I. Sergouniotis, F.S. Alkuraya, J.S.
989 Parboosingh, A.M. Innes, C.E. Willoughby, R.H. Giles, A.R. Webster, M. Ueffing, O.
990 Blacque, J.G. Gleeson, U. Wolfrum, P.L. Beales, T. Gibson, D. Doherty, H.M. Mitchison, R.
991 Roepman, and C.A. Johnson. 2015. An siRNA-based functional genomics screen for
992 the identification of regulators of ciliogenesis and ciliopathy genes. *Nat. Cell Biol.* 17:1074–
993 1087. doi:10.1038/ncb3201.

994 Winey, M., and E. O'Toole. 2014. Centriole structure. *Philos. Trans. R. Soc. B Biol. Sci.* 369.
995 doi:10.1098/rstb.2013.0457.

996 Wu, C.T., H.Y. Chen, and T.K. Tang. 2018. Myosin-Va is required for preciliary vesicle
997 transportation to the mother centriole during ciliogenesis. *Nat. Cell Biol.* 20:175–185.
998 doi:10.1038/s41556-017-0018-7.

999 Yang, T.T., W.M. Chong, W.J. Wang, G. Mazo, B. Tanos, Z. Chen, T.M.N. Tran, Y. De Chen,
1000 R.R. Weng, C.E. Huang, W.N. Jane, M.F.B. Tsou, and J.C. Liao. 2018. Super-resolution
1001 architecture of mammalian centriole distal appendages reveals distinct blade and matrix
1002 functional components. *Nat. Commun.* 9:1–11. doi:10.1038/s41467-018-04469-1.

1003 Ye, X., H. Zeng, G. Ning, J.F. Reiter, and A. Liu. 2014. C2cd3 is critical for centriolar distal

1004 appendage assembly and ciliary vesicle docking in mammals. *Proc. Natl. Acad. Sci. U. S.*
1005 *A.* 111:2164–2169. doi:10.1073/pnas.1318737111.

1006 Zimmermann, L., A. Stephens, S.Z. Nam, D. Rau, J. Kübler, M. Lozajic, F. Gabler, J. Söding,
1007 A.N. Lupas, and V. Alva. 2018. A Completely Reimplemented MPI Bioinformatics Toolkit
1008 with a New HHpred Server at its Core. *J. Mol. Biol.* 430:2237–2243.
1009 doi:10.1016/j.jmb.2017.12.007.

1010

Fig 1. CEP90 localizes to centriolar satellites and the distal tip of centrioles.

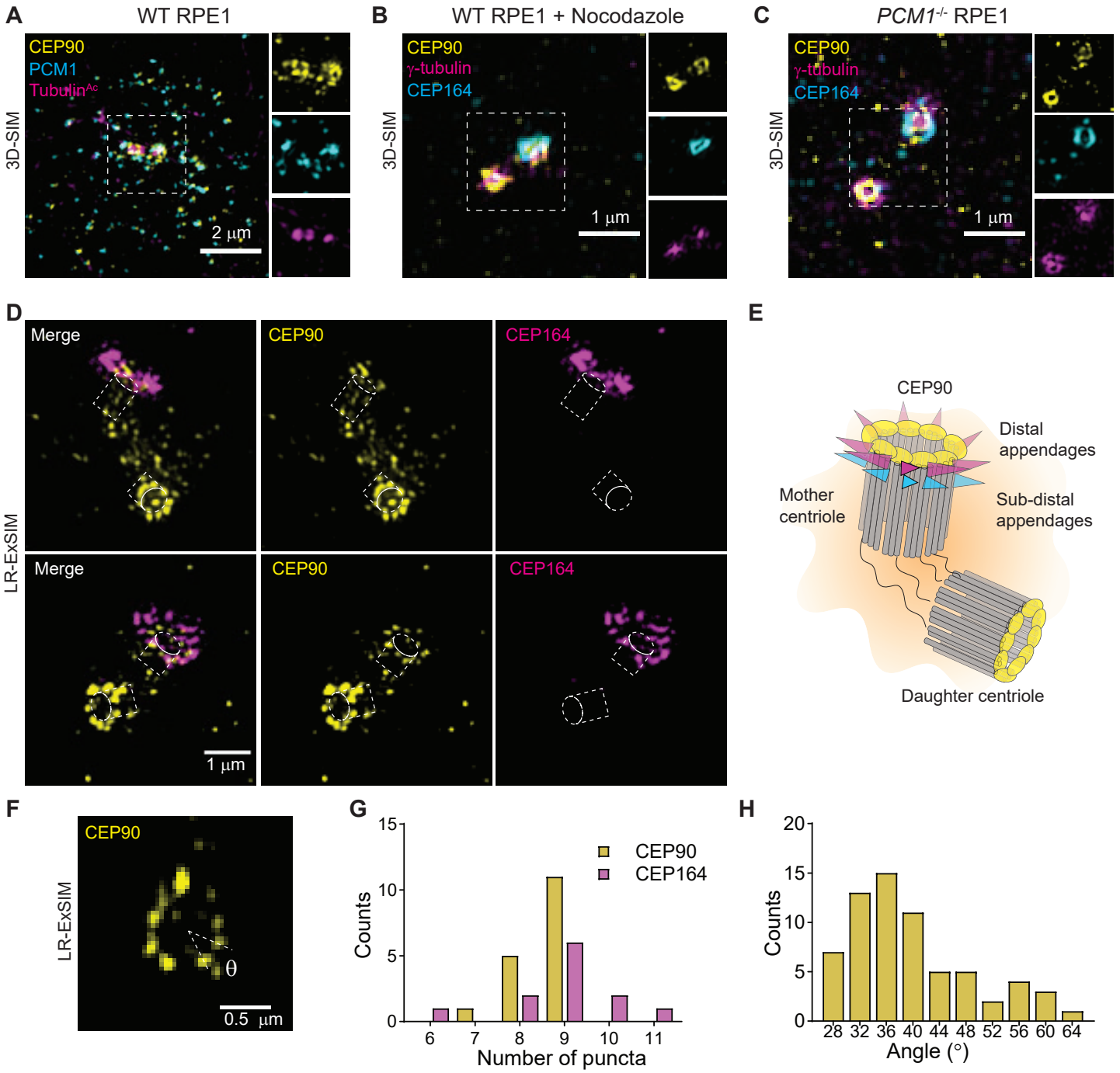

Fig 2. CEP90 forms a complex with OFD1 and MNR at the distal centriole

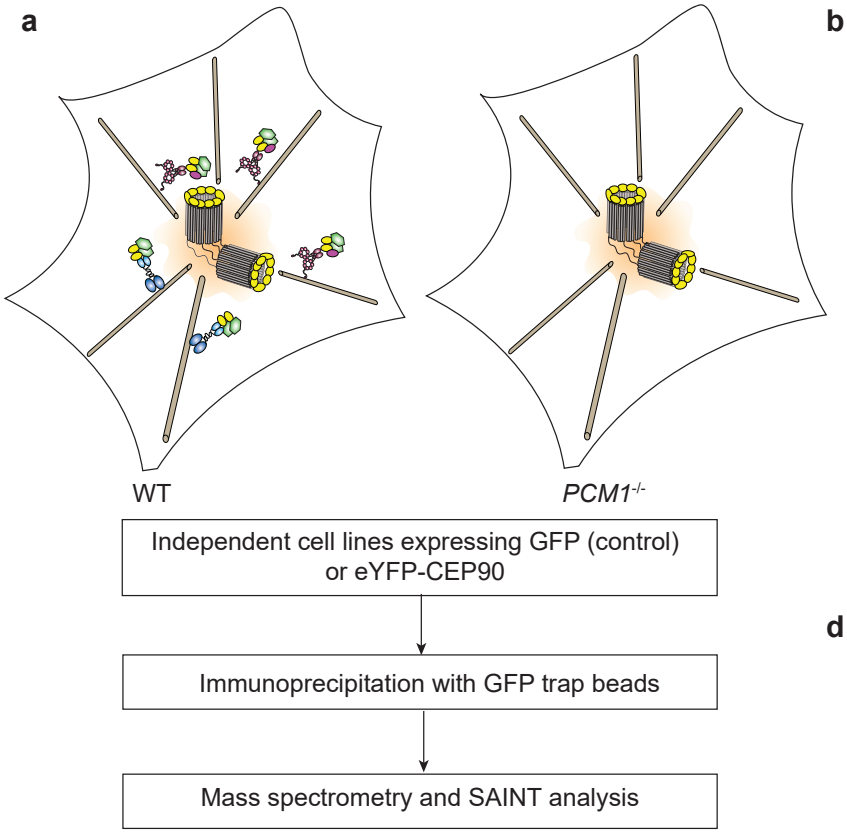

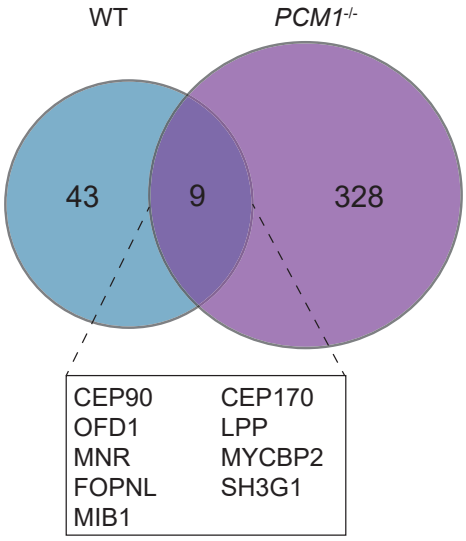

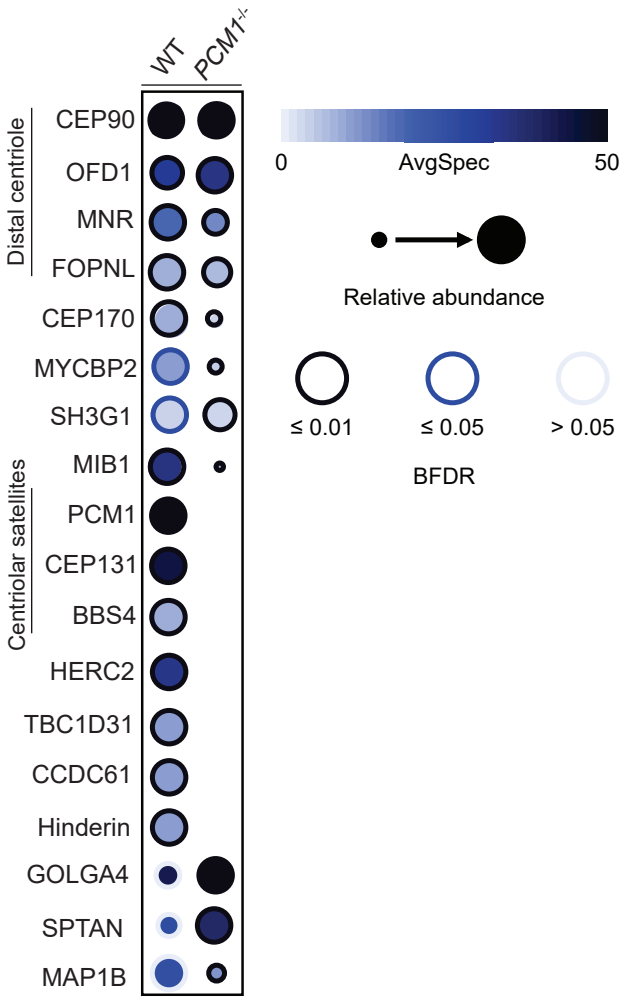

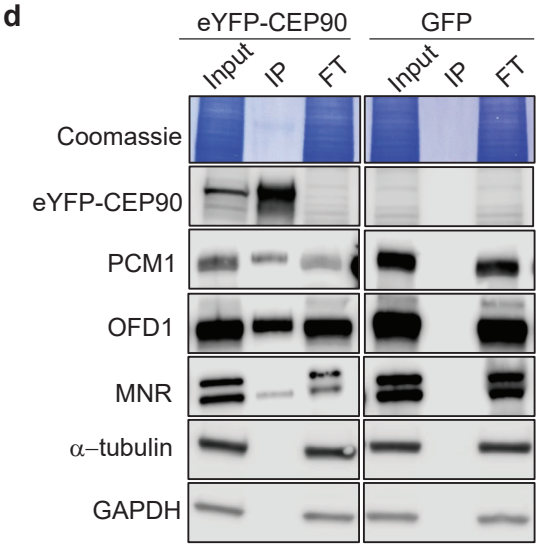

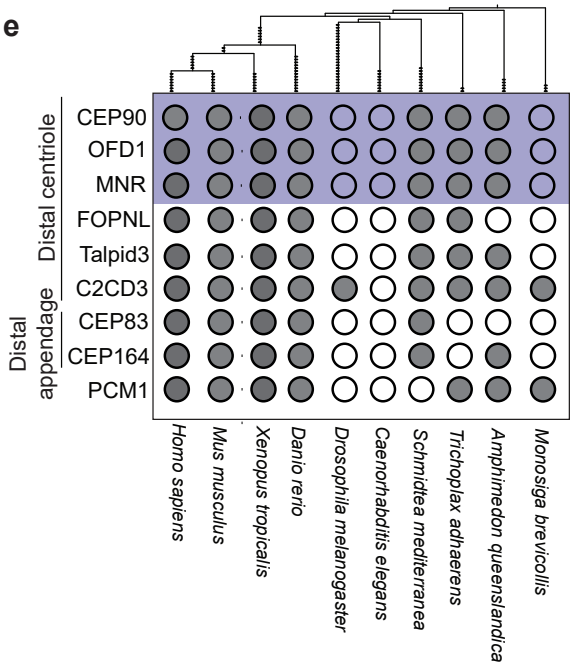

Fig 3. CEP90 colocalizes with OFD1 and MNR at centriolar satellites and at the distal centriole

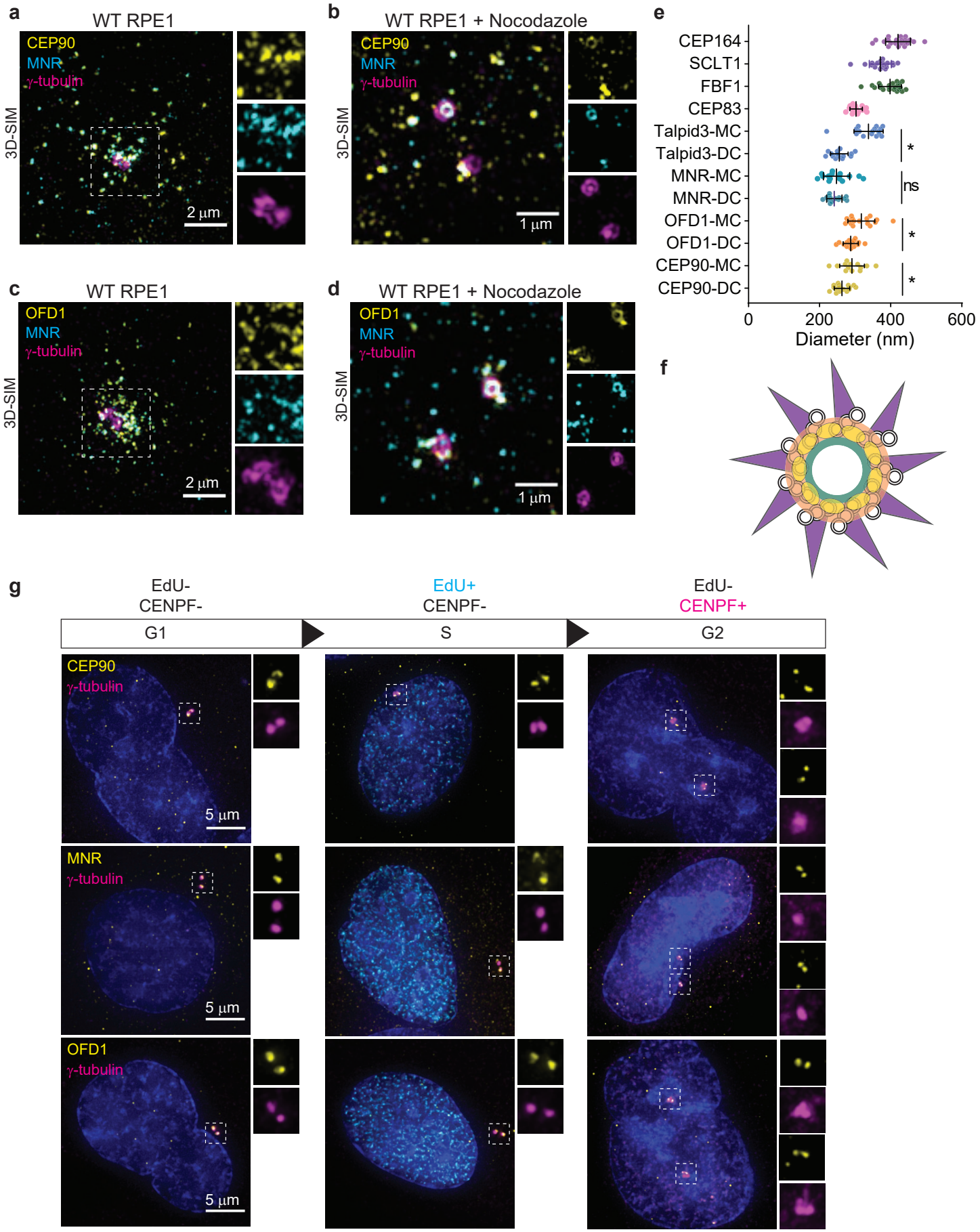

Fig 4. CEP90 and MNR are required for ciliogenesis

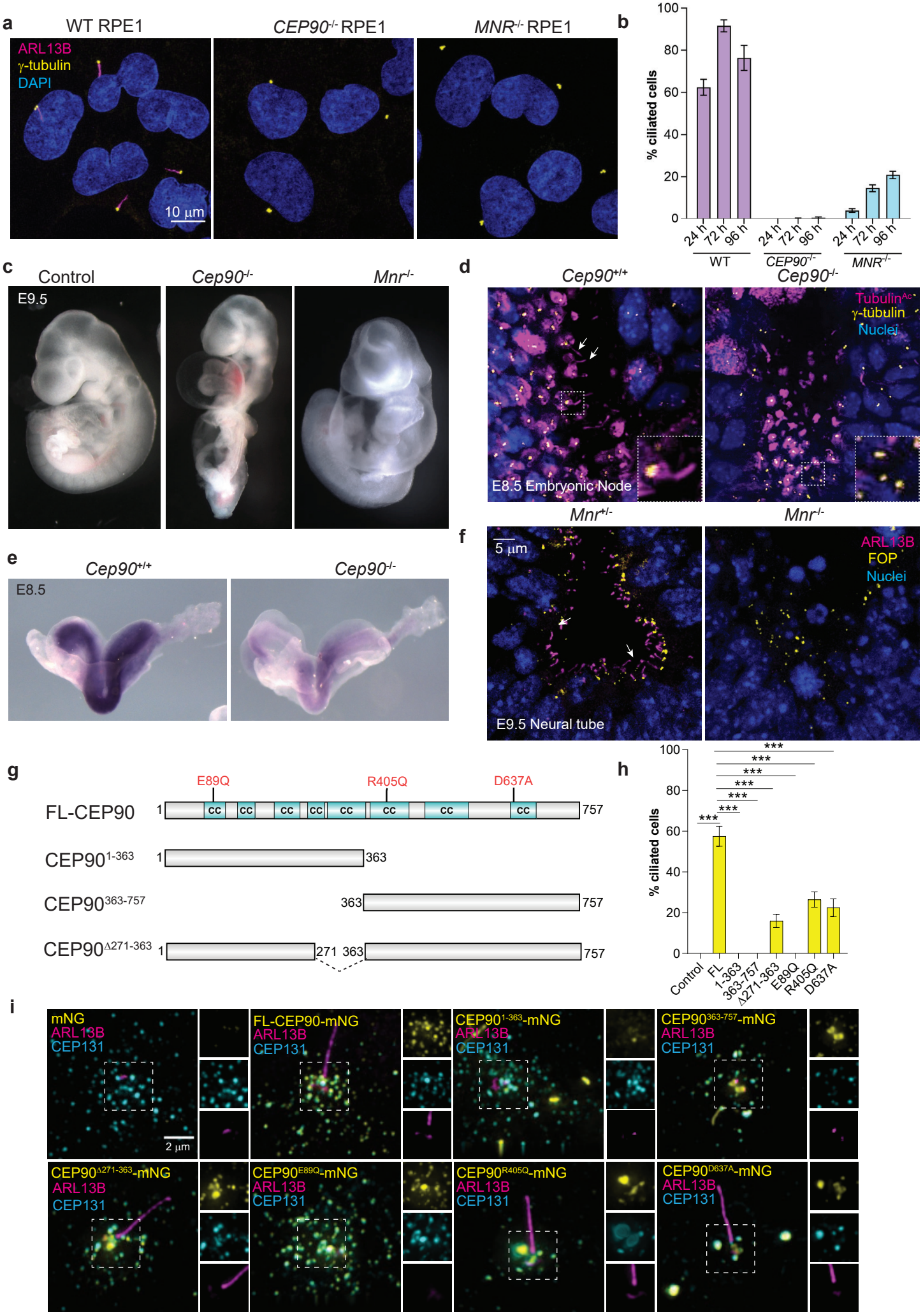

Fig 5. MNR, but not CEP90 restricts centriole length

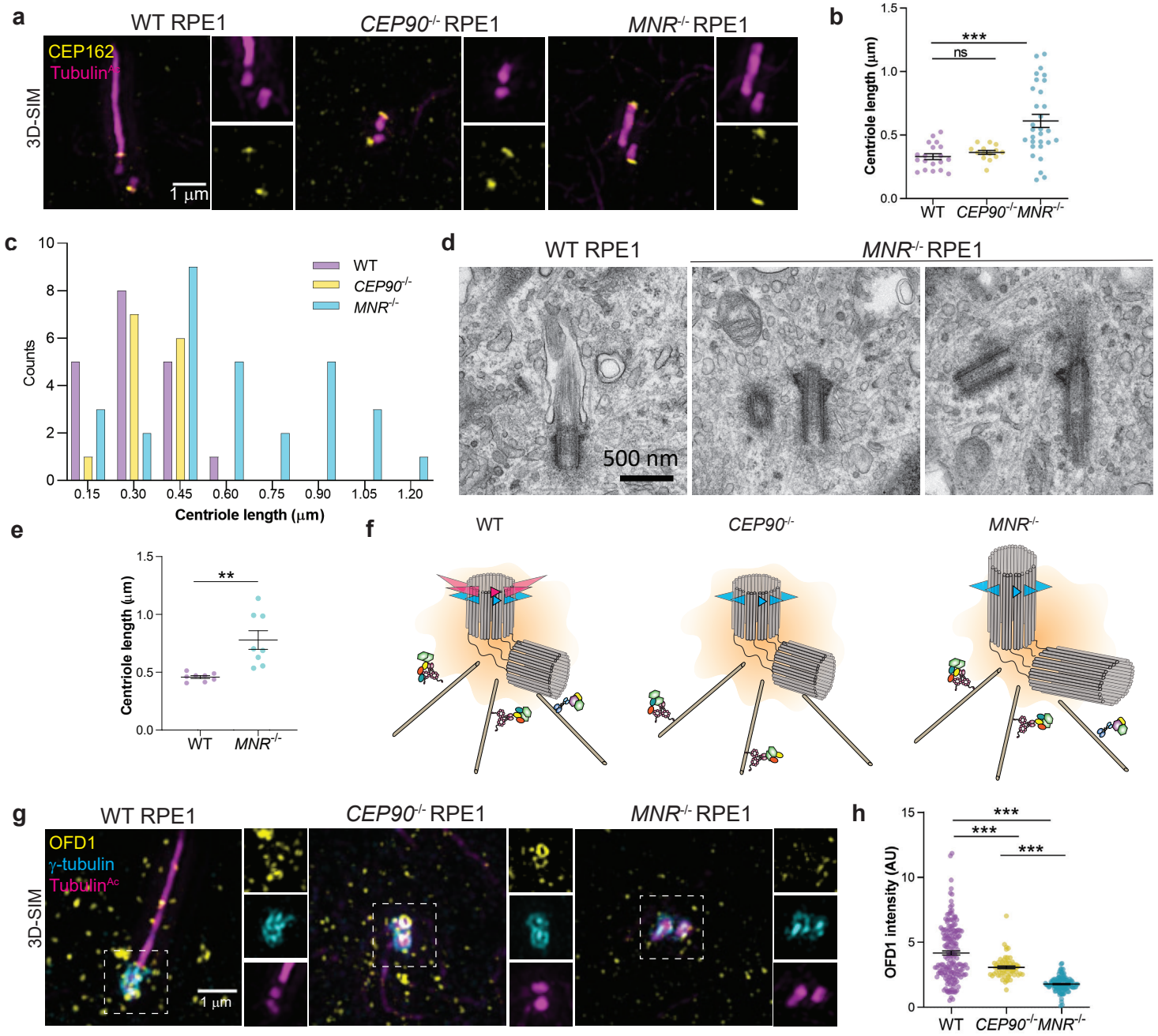

Fig 6. CEP90 and MNR are required for the early steps of ciliogenesis

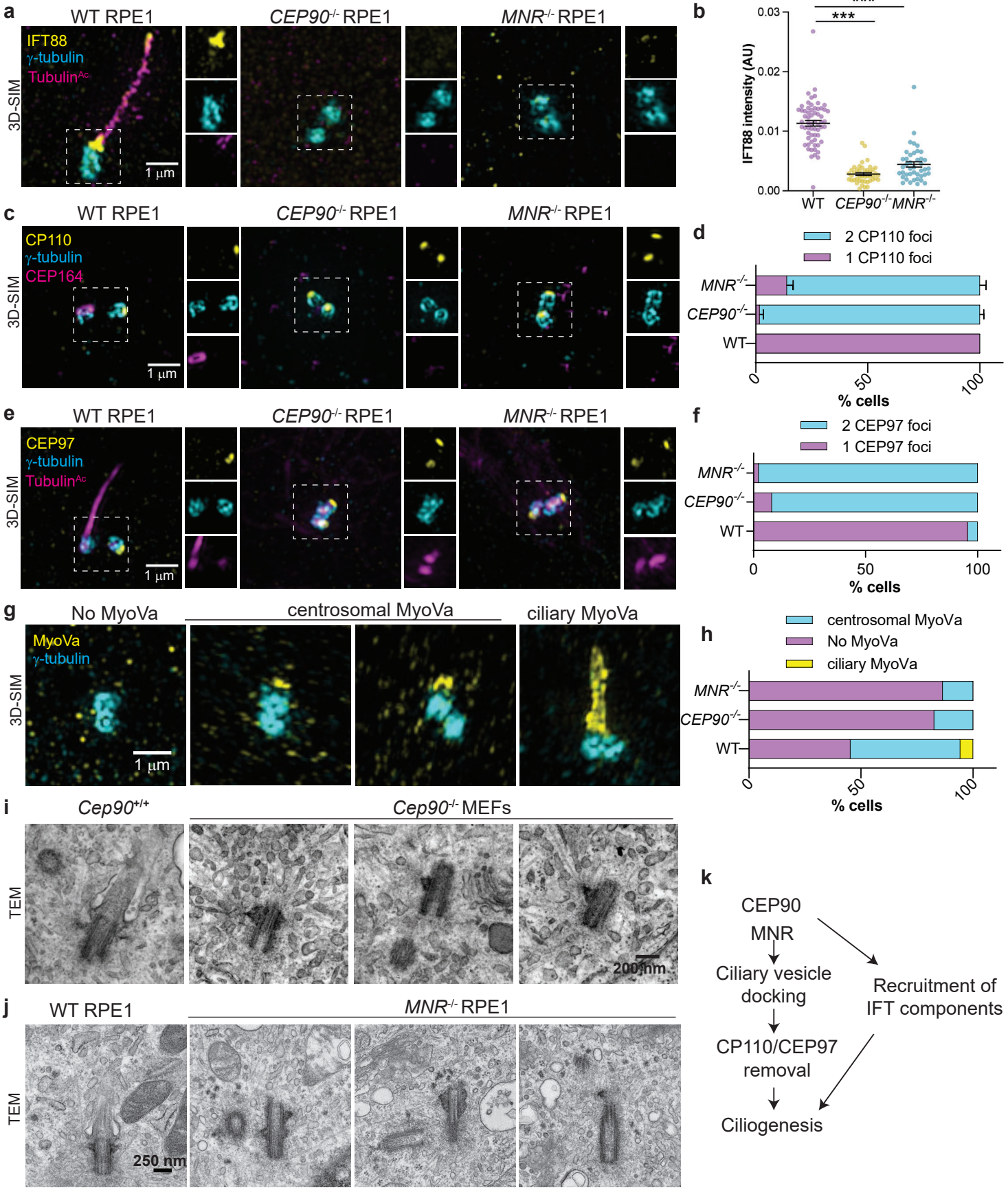

Fig 7. CEP90 and MNR are required for recruitment of distal appendage components to the mother centriole.

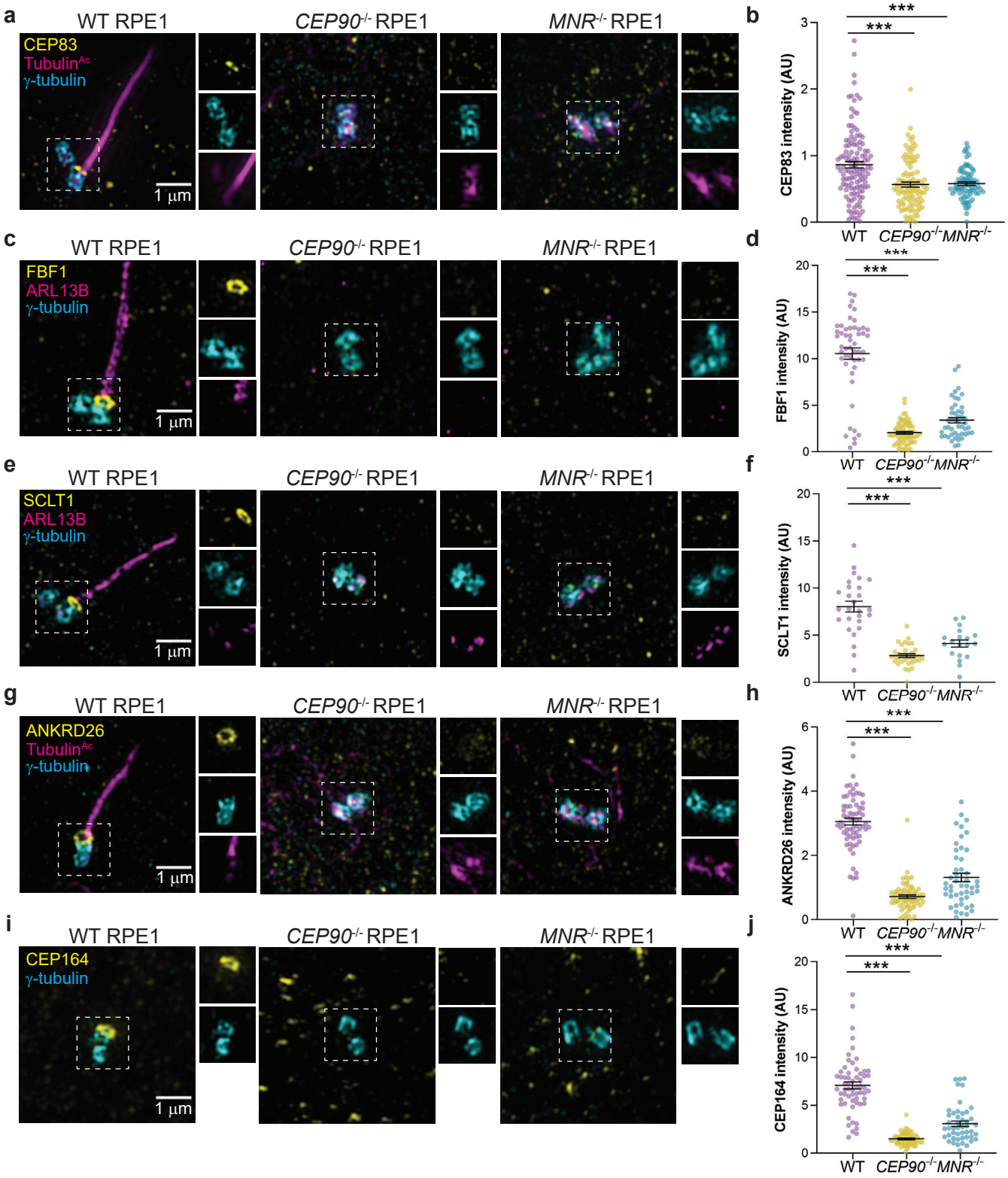

Fig 8. MNR recruits CEP90 which recruits CEP83 to build the distal appendage

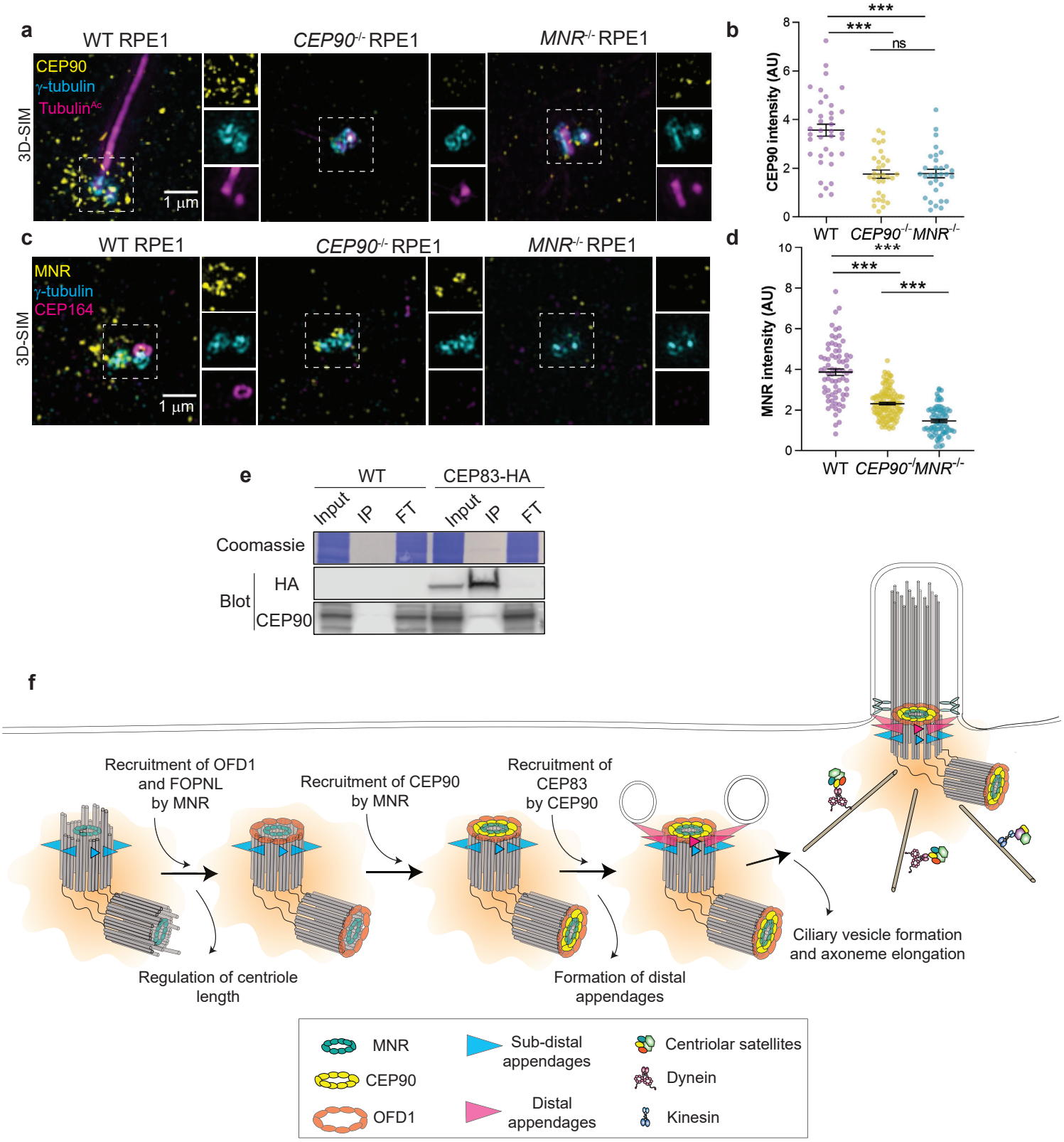

Supplementary Fig 1. Generation of *CEP90*$^{-/-}$, *MNR*$^{-/-}$ and *PCM1*$^{-/-}$ RPE1 cell lines

a *CEP90*$^{+/+}$ allele: 5'- TAGTTTAGAAACAACAGTTCCTACGGATGATATTTCCTCATCAGAAGAG -3'
CEP90$^{+/+}$ translate : MSRKISKESKKVNISSSLESEDISLETTVPTDDISSSEEREGKVRI----

CEP90$^{-/-}$ allele 1: 5'- TAGTTTAGAAACAACAGTTCCTA--|GATGATATTTCCTCATCAGAAGAG -3'
CEP90$^{-/-}$ allele 1 translate: MSRKISKESKKVNISSSLESEDISLETTVPR*

CEP90$^{-/-}$ allele 2: 5'- TAGTTTAGAAACAACAGTTCCTACG|--TGATATTTCCTCATCAGAAGAG -3'
CEP90$^{-/-}$ allele 2 translate: MSRKISKESKKVNISSSLESEDISLETTVPT*

b *MNR*$^{+/+}$ allele: 5'- TTTGATTCCTTCCTTTCCACCCTGTGTCGGGTATTTTATACTTAGTATGTC -3'
MNR$^{+/+}$ allele translate: MGPGQ---SSQKCGHTKYKIPDHRVERKESKSQAACQCSHQPSKVEISSSGAKVY----

MNR$^{-/-}$ allele 1: 5'- TTTGATTCCTTCCTTTCCACCCTGT|-GTCGGGTATTTTATACTTAGTATGTC -3'
MNR$^{-/-}$ allele 1 translate: MGPGQ---SSQKCGHTKYKIPDTGWKGRNQRVKQPVSVATSHPK*

MNR$^{-/-}$ allele 2: 5'- TTTGATTCCTTCCTTTCCACCCTGT|NGGTCGGGTATTTTATACTTAGTATGTC -3'
MNR$^{-/-}$ allele 2 translate:MGPGQ---SSQKCGHTKYKIPDXQGGKEGIKESSSLSV*

c *PCM1*$^{+/+}$ allele : 5'- GATCATCAGAAAAGAATAAGAAAAAGTTTGGTGTAGAAAGTGATAAAAGAG -3'
PCM1$^{+/+}$ allele translate: MATGGGPFEDGMNDQDLPNWSNENVDDRLNNMDWGAQQKKANRSSEKNKKKFGVES---

PCM1$^{-/-}$ allele : 5'- GATCATCAGAAAAGAATAAGAAAAA|NGTTTGGTGTAGAAAGTGATAAAAGAG -3'
PCM1$^{-/-}$ allele translate: MATGGGPFEDGMNDQDLPNWSNENVDDRLNNMDWGAQQKKANRSSEKNKKXVWCRK*

PAM site
Cut site
- = deletion
N = insertion
* = stop codon

d

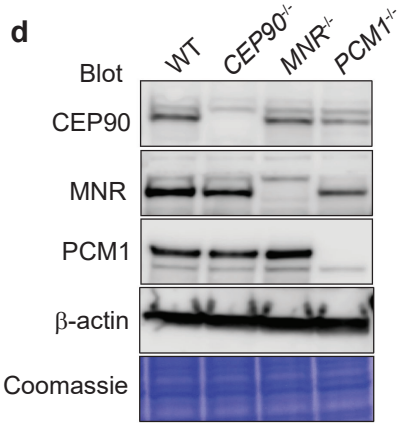

Supplementary Fig 2. Overexpressed MNR localizes to microtubules, and recruits endogenous OFD1

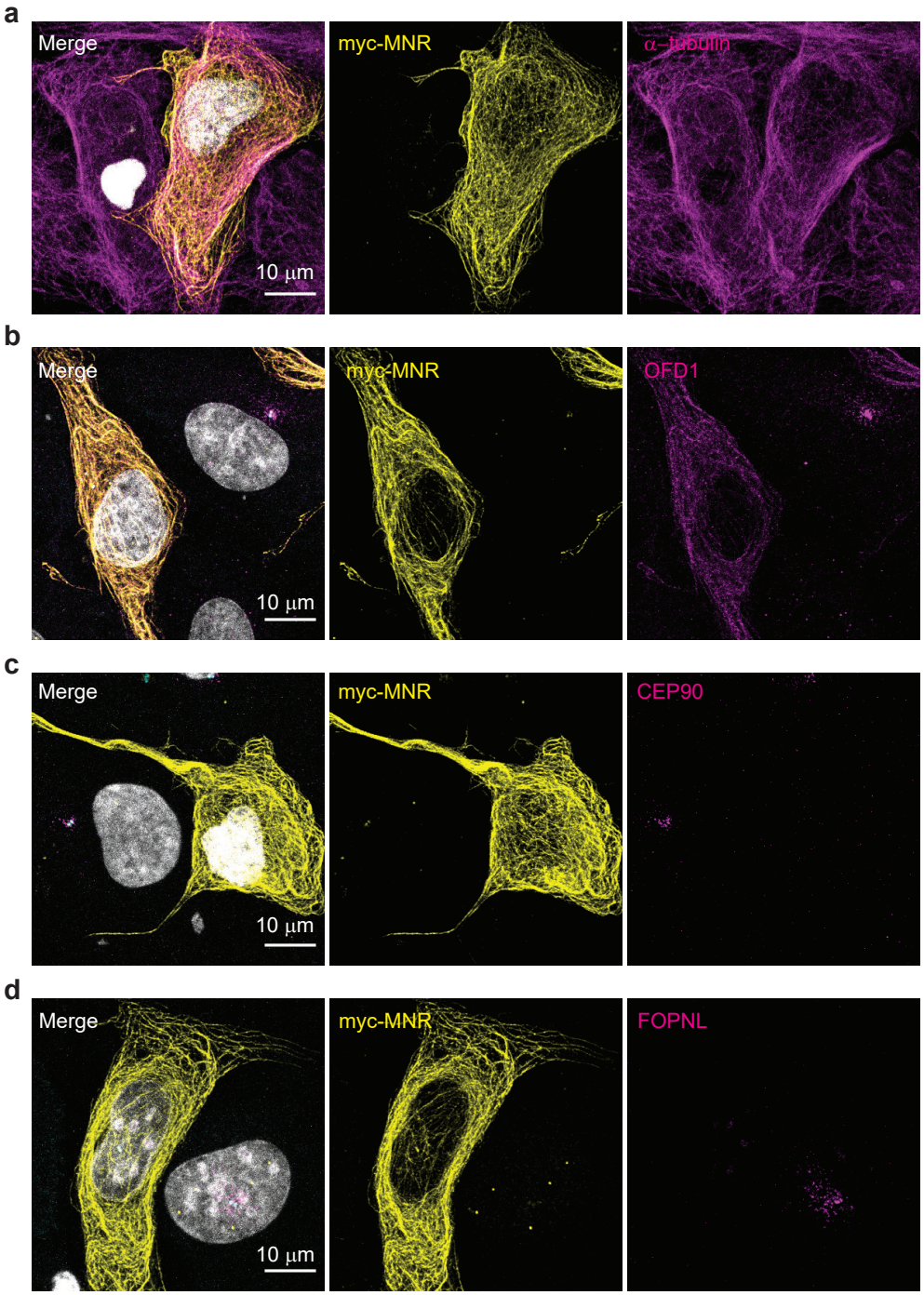

Supplementary Fig 3. CEP90 and MNR regulate distal appendage assembly independent of Talpid3 recruitment and removal of Centrobin.

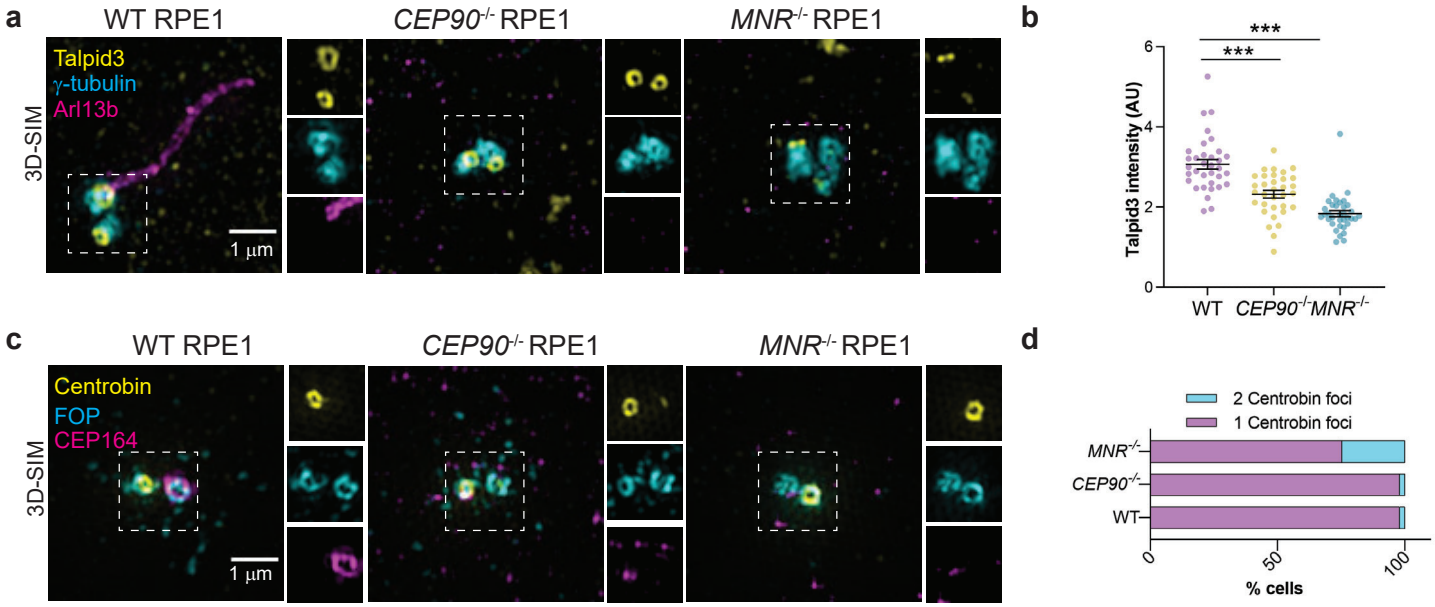

Supplementary Fig 4. Serial section TEM of WT and *Cep90*$^{-/-}$ MEF cells.

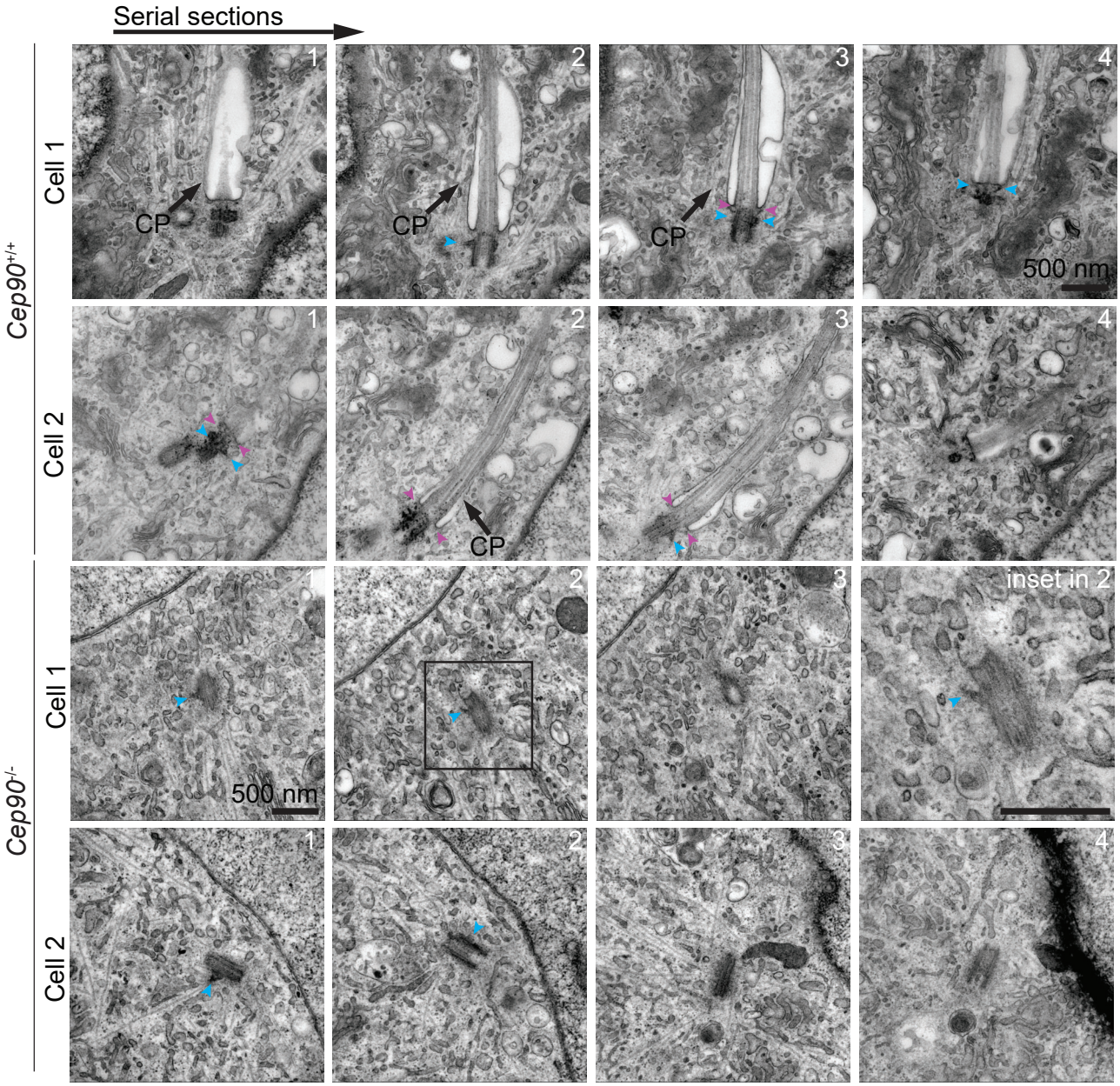

Supplementary Fig 5. Serial section TEM of WT and *MNR*$^{-/-}$ RPE1 cells.

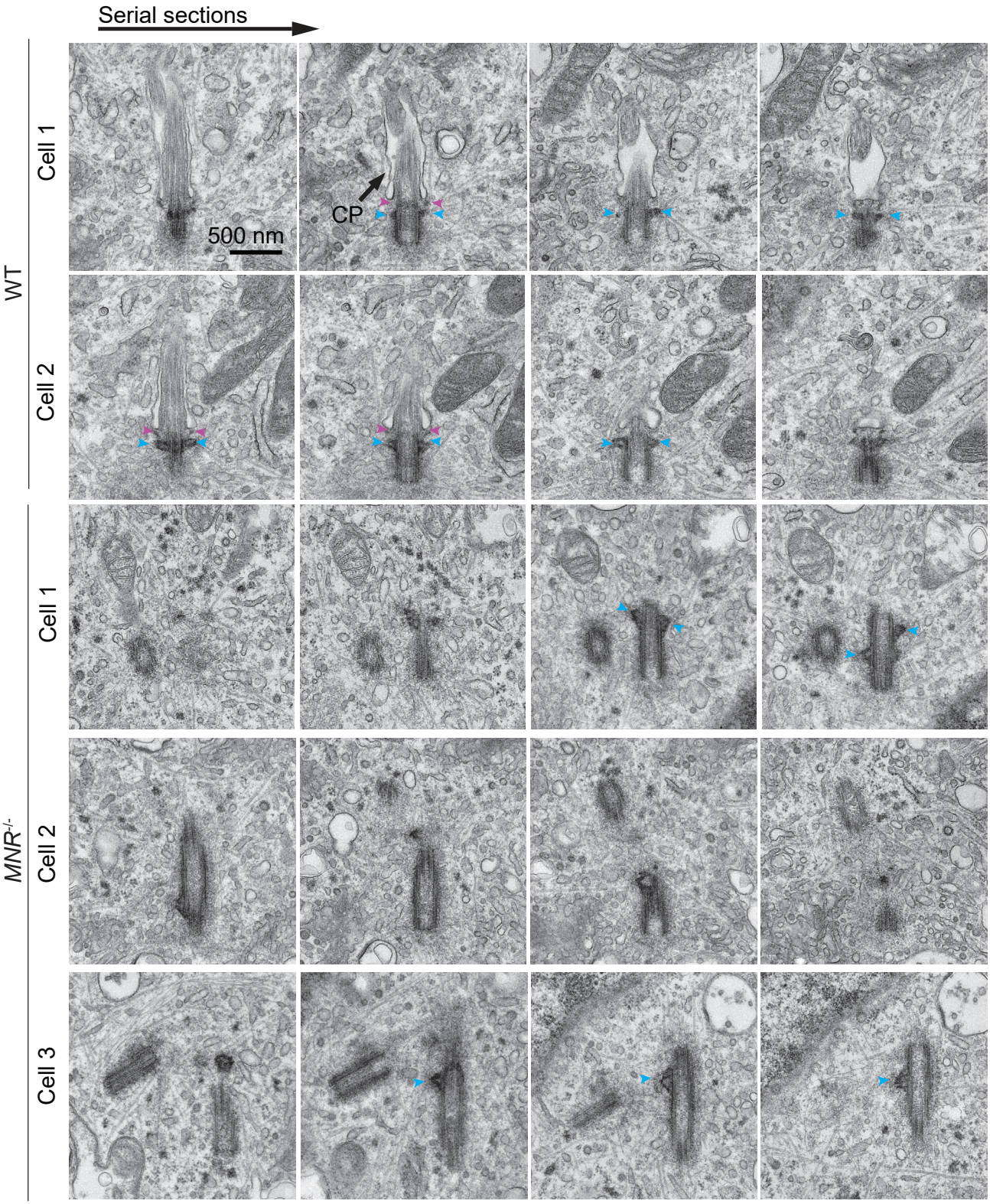

Supplementary Fig 6. Components of sub-distal appendages are recruited to the mother centriole in the absence of CEP90 and MNR

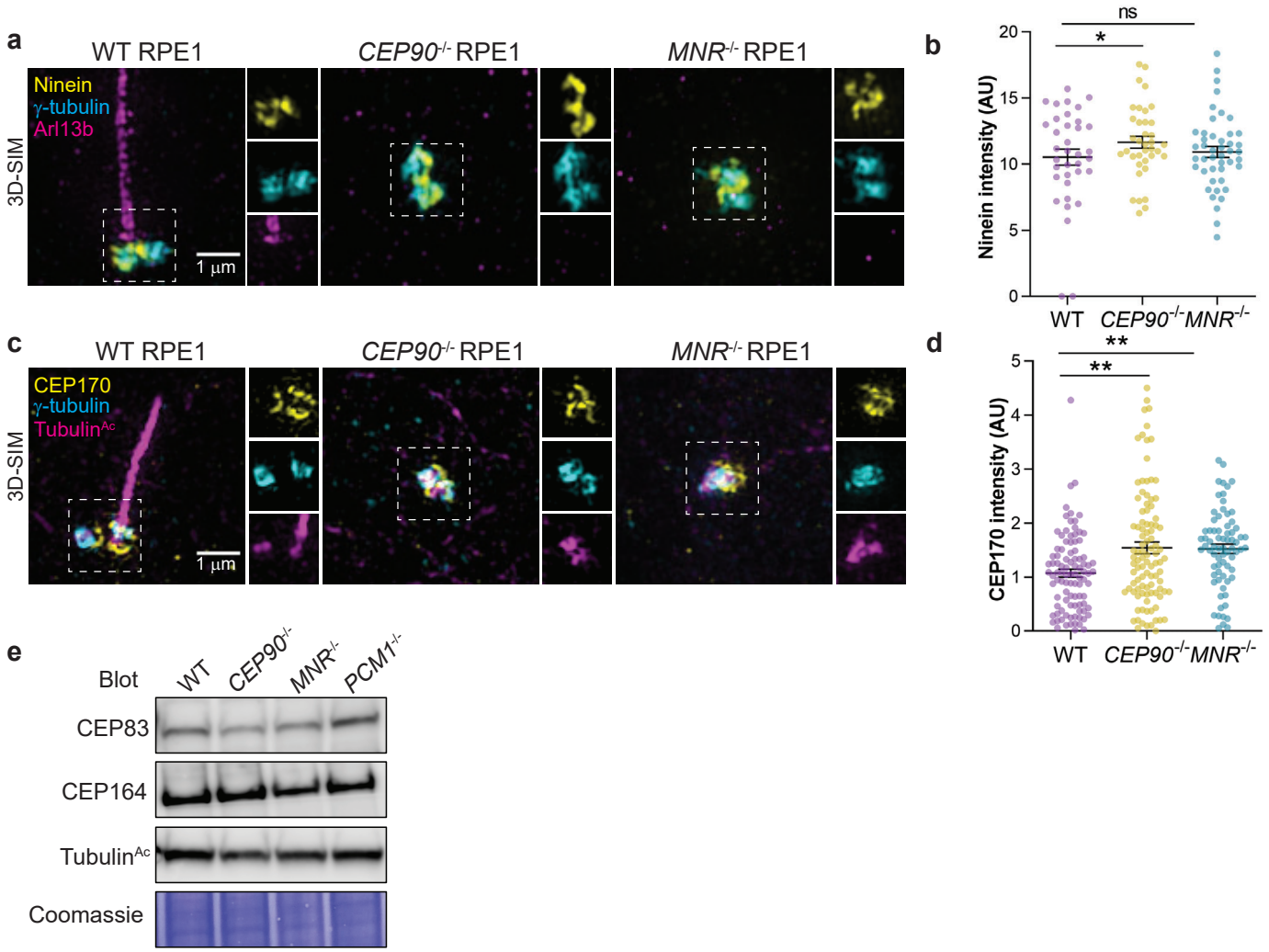

Supplementary Fig 7. Centriolar satellites are dispensable for distal appendage assembly at the mother centriole

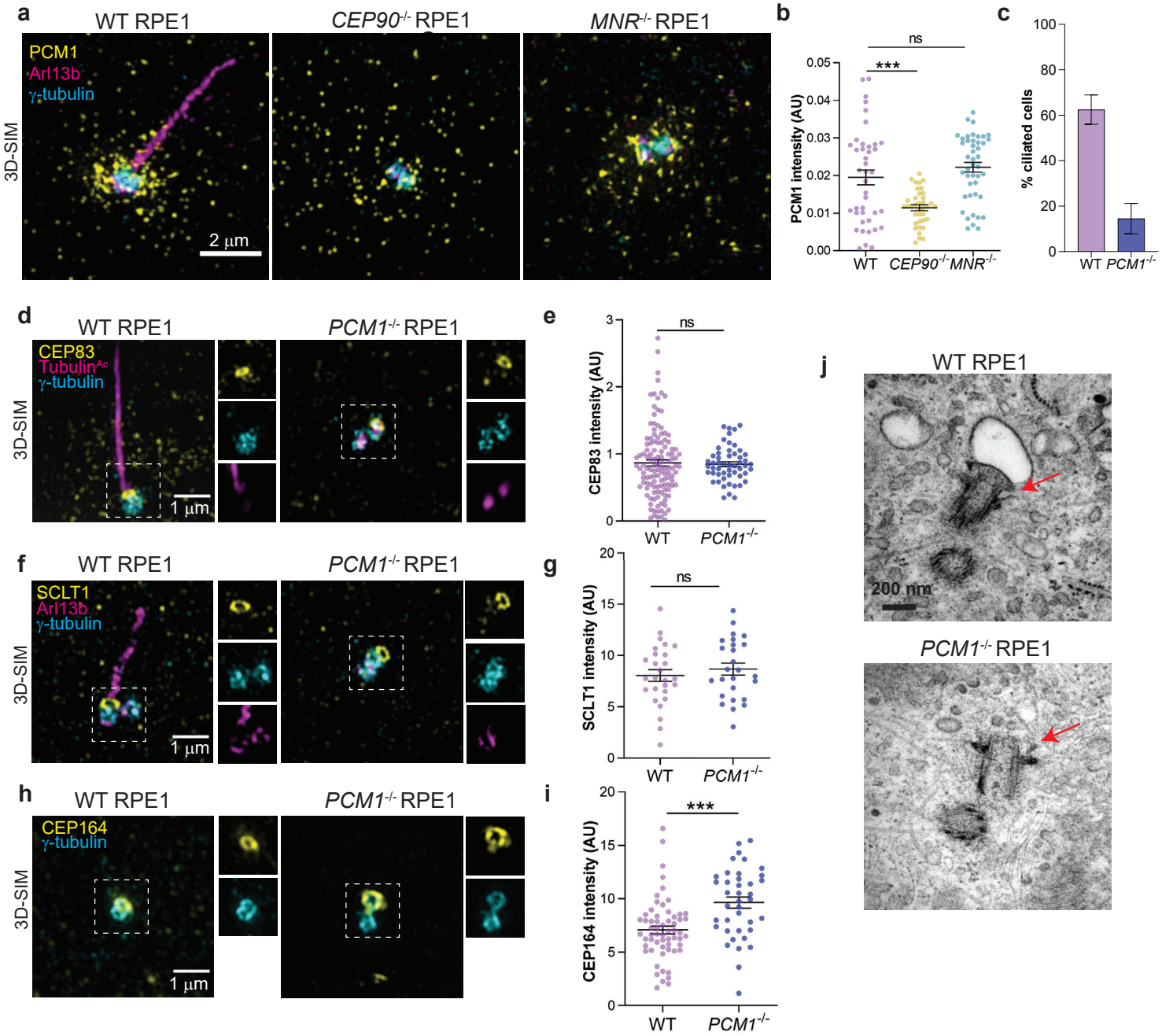

Table 1. List of primary antibodies used in this study for immunofluorescence (IF) and western blotting (WB)

Antibody	Host	Source	Catalog Number	Dilution/Fixation (IF)	Dilution (WB)
CEP90	Rabbit	Proteintech	14413-1-AP		1:500
CEP90	Rabbit	Kunsoo Rhee[1]		1:500/MeOH	
MNR	Rat	Olivier Rosnet[2]		1:500/MeOH	
MNR	Rabbit	Novus Biologicals	NBP1-90929		1:500
OFD1	Rabbit	Novus Biologicals	NBP1-89355	1:500/MeOH	1:500
FOPNL	Rabbit	Sigma Prestige	HPA040599	1:100/MeOH	
CEP164	Goat	Santa Cruz Biotechnology	sc-240226	1:100/MeOH	
CEP164	Mouse	Novus Biologicals	NBP2-43707		1:2000
γ-tubulin	Mouse	Sigma GTU-88	T6557	1:500/MeOH	
Tubulin^{Ac}	Rabbit	Cell Signaling Technology	5335T	1:2000/MeOH	
Tubulin^{Ac}	Mouse	Santa Cruz Biotechnology	sc-23950 AF647	1:100/MeOH	
α-tubulin	Mouse	Sigma Aldrich	T5168	1:1000/PFA	
β-actin	Mouse	Proteintech	6008-1-Ig		1:100,000
GAPDH	Mouse	Proteintech	60004-1-Ig		1:100,000
FBF1	Rabbit	Proteintech	11531-1-AP	1:100/MeOH	
ANKRD26	Rabbit	GeneTex	GTX128255	1:100/MeOH	
CEP83	Rabbit	Sigma Prestige	HPA038161	1:100/MeOH	
CENPF	Mouse	BD Biosciences	610768	1:100/MeOH	
Myo-Va	Rabbit	Novus Biologicals	NBP1-92156	1:100/MeOH	
CP110	Mouse	Millipore	MABT1354	1:100/MeOH	
CEP97	Rabbit	Proteintech	22050-1-AP	1:100/MeOH	
IFT88	Rabbit	Proteintech	13967-1-AP	1:100/MeOH	
FOP	Rabbit	Proteintech	11343-1-AP	1:500/MeOH/ PFA	
PCM1	Rabbit	Proteintech	19856-1-AP		1:500
PCM1	Mouse	Santacruz	sc-398365	1:100/MeOH	
Talpid3	Rabbit	Proteintech	24421-1-AP	1:100/MeOH	
Centrobin	Mouse	Abcam	Ab70448	1:100/MeOH	
Ninein	Rabbit	Michel Bornens	L79	1:200/MeOH	
ODF2	Mouse	Novus Biologicals	H00004957-M01	1:100/MeOH	
CEP170	Mouse	ThermoFisher	72-413-1	1:100/ MeOH	
Myc-tag	Goat	Novus Biologicals	NB600-335	1:500/PFA	
Arl13b	Rabbit	Proteintech	177100-1-AP	1:500/MeOH/ PFA	
mNeonGreen	Mouse	Chromotek	32F6	1:500/PFA	
Talpid3	Rabbit	Proteintech	24421-1-AP	1:100/MeOH	
CEP162	Rabbit	Sigma Prestige	HPA030170	1:100/MeOH	
CEP131	Guinea pig	Kodani et al.,2015 [3]		1:100/PFA/ MeOH	